ACSNANO

www.acsnano.org

ARTICLE

Patterning of Self-Assembled Monolayers of Amphiphilic Multisegment Ligands on Nanoparticles and Design Parameters for Protein Interactions

Samuel E. Hoff, Desiré Di Silvio, Ronald F. Ziolo, Sergio E. Moya, and Hendrik Heinz*

Cite This: *ACS Nano* 2022, 16, 8766–8783

Read Online

ACCESS | Metrics & More | Article Recommendations | Supporting Information

ABSTRACT: Functionalization of nanoparticles with specific ligands is helpful to control specific diagnostic and therapeutic responses such as protein adsorption, cell targeting, and circulation. Precision delivery critically depends on a fundamental understanding of the interplay between surface chemistry, ligand dynamics, and interaction with the biochemical environment. Due to limited atomic-scale insights into the structure and dynamics of nanoparticle-bound ligands from experiments, relationships of grafting density and ligand chemistry to observable properties such as hydrophilicity and protein interactions remain largely unknown. In this work, we uncover how self-assembled monolayers (SAMs) composed of multisegment ligands such as thioalkyl-PEG-(*N*-alkyl)amides on gold nanoparticles can mimic mixed hydrophobic and hydrophilic ligand coatings, including control of patterns, hydrophilicity, and specific recognition properties. Our results are derived from molecular dynamics simulations with the INTERFACE-CHARMM36 force field at picometer resolution and comparisons to experiments. Small changes in ligand hydrophobicity, via adjusting the length of the N-terminal alkyl groups, tune water penetration by multiples and control superficial ordering of alkyl chains from 0 to 70% regularity. Further parameters include the grafting density of the ligands, curvature of the nanoparticle surfaces, type of solvent, and overall ligand length, which were examined in detail. We explain the thermodynamic origin of the formation of heterogeneous patterns of multisegment ligand SAMs and illustrate how different degrees of ligand order on the nanoparticle surface affect interactions with bovine serum albumin. The resulting design principles can be applied to a variety of ligand chemistries to customize the behavior of functionalized nanoparticles in biological media and enhance therapeutic efficiency.

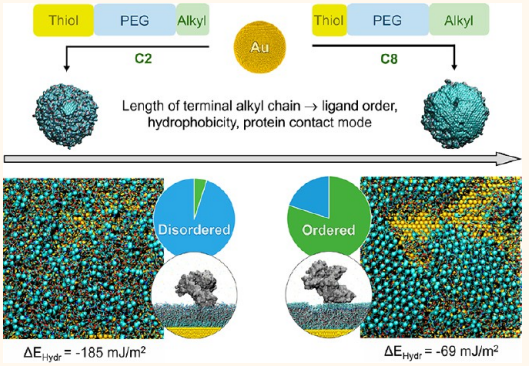

KEYWORDS: *nanoparticles, self-assembled monolayers, multisegment ligands, molecular dynamics simulation, ligand patterns, nanoparticle solubility, protein recognition*

Nanoparticles (NPs) are used to diagnose and treat a broad range of medical conditions and have great promise to overcome limitations of conventional delivery.[1] The surface chemistry hereby plays a critical role to control interactions in biological environments.[2,3] The affinity of the nanoparticle and surface-grafted ligands to ions, proteins, polysaccharides, and other molecules in physiological surroundings typically leads to the formation of a corona that is composed of diverse species. The corona can greatly affect the biodistribution of the nanoparticles and modify barriers to cargo delivery, translocation across cell membranes, side reactions, and other stimuli-driven interactions in biological environments.[4−8] Customization of the nanoparticle surface is therefore important to tailor functional properties, including colloidal stability and circulation time. In this contribution, we examined how a multiblock structure of the ligands as well as changes in hydrophobicity and grafting density affect the assembly, order, and dynamics at the molecular scale. We quantify changes in hydration energies and interaction with proteins. The results reveal design parameters that control the structure of ligand−solution interfaces and may be helpful to

Received: October 2, 2021
Accepted: May 17, 2022
Published: May 22, 2022

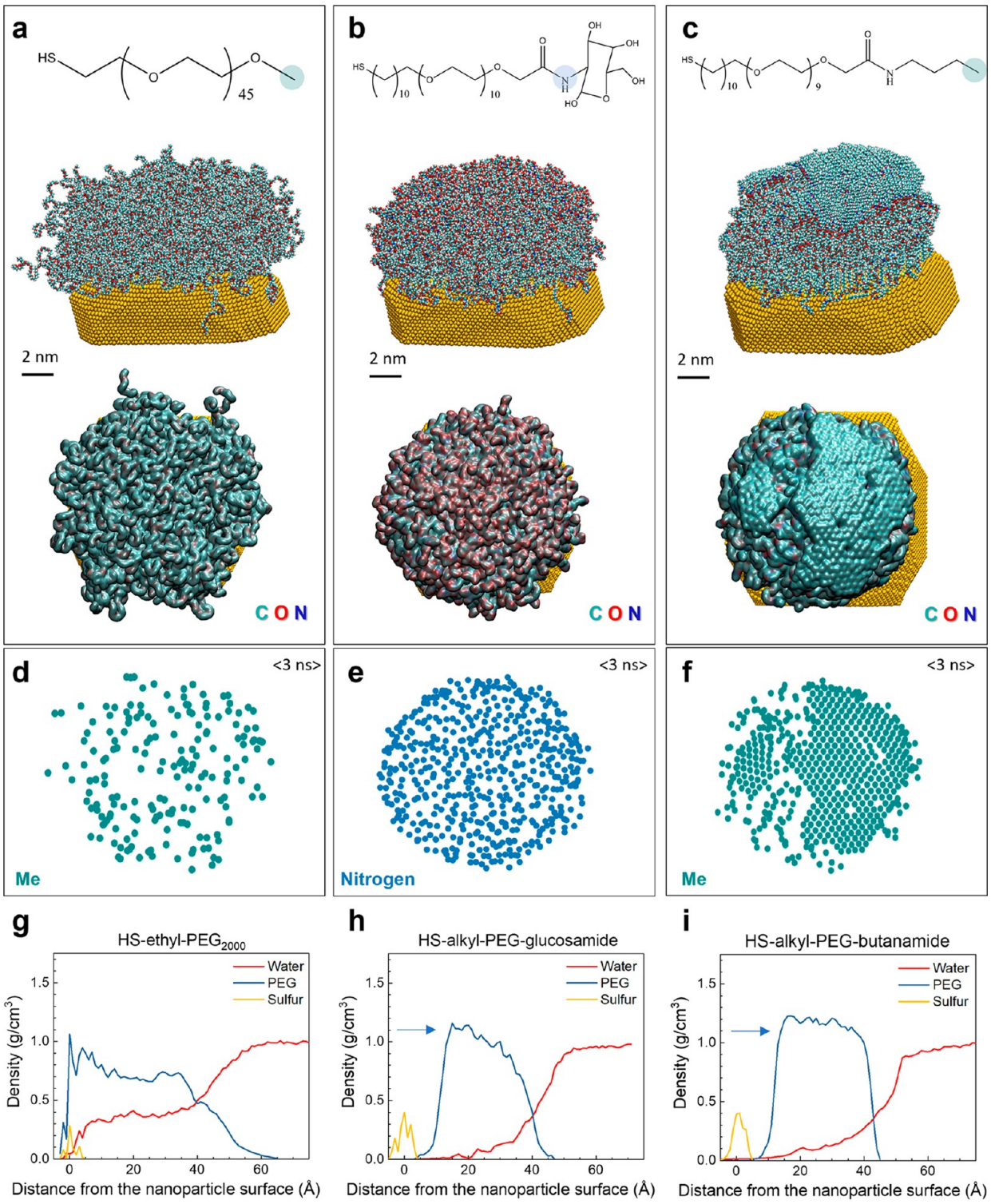

Figure 1. Differences in organization and dynamics of HS-ethyl-PEG$_{2000}$, HS-alkyl-PEG-(*N*-glucosyl)acetamide (APG), and HS-alkyl-PEG-(*N*-butyl)acetamide (APB) coatings on a sliver of a 20 nm diameter Au nanoparticle. The chosen grafting densities represent common saturation values observed in experiments. (a) Side and top views of HS-ethyl-PEG$_{2000}$ (MW 2000 g/mol) at 1.5 chains per nm^2 (refs 58 and 59). (b) HS-alkyl-PEG-(*N*-glucosyl)acetamide at 4.2 chains per nm^2 (refs 56 and 57) and (c) HS-alkyl-PEG-(*N*-butyl)acetamide at 4.2 chains per nm^2 (refs 56 and 57). (d) Average position of the terminal methyl group (C atom) of PEG$_{2000}$, (e) amide nitrogen atom in APG, and (f) terminal methyl group in APB. Density profiles of surface-bound sulfur atoms, PEG chains, and water molecules as a function of radial distance for (g) PEG$_{2000}$, (h) APG, and (i) APB ligands. Blue arrows in (h,i) highlight differences in PEG density and orientation. The PEG density decreases continuously as a function of distance for *N*-glucosyl termination, including many different orientations, and remains steady for *N*-butyl termination.

engineer nanoparticle−protein aggregates and their destiny in biological systems.

Previous studies have shown that surface functionalization of the nanoparticles through ligands correlates with the extent of

https://doi.org/10.1021/acsnano.1c08695
ACS Nano 2022, 16, 8766−8783

intracellular aggregation of the nanoparticles, as well as the protein corona composition, and offers a promising route to improve therapeutic functions.[9,10] While customized ligands offer a path to control the properties of the ligand corona and thus the fate of nanoparticles in vivo, a strong correlation with chemical composition, grafting density, length, and, particularly, ligand heterogeneity on the NP surface is known.[11−14] Several studies demonstrate that small changes in ligand structure and dynamics can have significant impact on nanoparticle interaction with biomolecules.[15−17] However, it remains difficult to identify and control the variables which alter ligand properties, the associated dynamics, and organization. A major challenge is that current experimental techniques cannot monitor soft matter−solution interfaces at atomic resolution over the involved time scales. In addition, the number of variables that impact nanoparticle fate in biological environments is quite large, so that a combination of experimental and in silico techniques is helpful. Experimental data on nanoparticle composition and tracking, tests of therapeutic efficacy and toxicity, as well as mechanistic hypotheses in complex in vitro and in vivo experiments can then be combined with high-resolution modeling of ligand structures, dynamics, and theoretical models to faster elucidate how ligand chemistry and structure affect nanoparticle fate and performance.

Molecular dynamics simulation, in particular, has been instrumental to collect information on the structure and dynamics of self-assembled monolayers (SAMs) of ligands at nanoparticle interfaces.[18−22] SAMs comprising alkanethiol or poly(ethylene glycol) (PEG)-based ligands are also of interest for applications in catalysis, electrochemistry, and antifouling coatings.[23−30] However, simulations to date have not examined the dynamics of SAMs comprising a singular type of multisegment ligands such as alkanethiols terminated with PEG and additional functional groups,[31] which have shown promise in experiments to control protein interactions with surfaces.[32−34]

Instead, attention has been given to SAMs of mixed ligands in experimental and computational studies due to the spontaneous formation of phase-separated nanoscale domains on nanoparticle surfaces.[35−38] Mixtures of hydrophilic and hydrophobic ligands thus have the potential to undergo phase separation into hydrophilic and hydrophobic regions.[39] Alternating regions of mixed SAMs with such properties on nanoparticles are believed to have a large impact on protein adsorption and NP−membrane interactions.[40−42] For example, changing the hydrophilic/hydrophobic domain size and structure would modify hydrophilicity and recognition properties, allowing some control over the affinity toward proteins, including binding modes, NP fate, and toxicity.[39,43,44] However, the existence of such nanopatterned ligand structures has been challenged in experiments.[45−47] Monte Carlo and coarse-grained MD simulations have also suggested the instability of ligand mixtures.[48,49] For example, the stripe-like features observed for mixed SAMs may only be a transition state before forming Janus-like nanoparticles or homogeneous mixed coatings on the NP surface. Whether the structures formed by SAMs of mixed ligands are stable or not, a robust method to functionalize nanoparticle surfaces with tunable ratios of distinct functional groups displayed at the ligand−liquid interface has great promise to precision engineer nanoparticle interactions in biological environments.

In this contribution, we demonstrate the spontaneous formation of ordered hydrophobic and disordered hydrophilic phases of SAMs of amphiphilic multisegment ligands on Au nanoparticles and flat Au surfaces using molecular dynamics (MD) simulation with thoroughly validated models, namely, the INTERFACE force field (IFF) in combination with CHARMM36 parameters.[50−55] The multisegment ligands incorporate the desired chemical specificities into single ligands, which reduces or eliminates the odds of instability and disassembly of SAMs comprising mixed ligands. Using block-type HS-alkyl-PEG-(*N*-alkyl)acetamide ligands with 62−100% of the typical surface coverage,[56−60] we found that the presence of N-terminal alkyl end groups of a specific length enables phase segregation into ordered and disordered regions at nanoparticle−solution interfaces. The SAMs with multisegment ligands can thus expose either hydrophobic or hydrophilic domains, similar to observations for immiscible dual-component SAMs.[36] We describe precise tuning of the amount of ordered and disordered phases of HS-alkyl-PEG-(*N*-alkyl)acetamide ligands at a given grafting density by altering the length of the terminal alkyl chain. We explain the organization of such PEG-based ligands on gold surfaces as a function of differences in grafting density, chemistry of terminal functional groups, and ligand hydrophobicity, as well as solvent polarity at picometer resolution, including a conceptual thermodynamic model that rationalizes the formation of two phases. We also tested the effects of structural changes in the ligand-modified NP surface on interactions with proteins in solution using the example of bovine serum albumin (BSA). The findings from MD simulations and comparisons to available experimental data indicate that tuning the hydrophilicity of multisegment ligands is a promising strategy to customize protein−nanoparticle interactions and nanoparticle fate in biological media.

RESULTS AND DISCUSSION

Structure and Dynamics of Single-Segment and Multisegment Thiol-PEG-Based Ligand Monolayers on Au. We characterized three distinct ligand coatings on a part of the surface of a spherical Au nanoparticle of 20 nm diameter, including ethylthiol-PEG_{2000}, alkylthiol-PEG-(*N*-glucosyl)-acetamide (APG), and alkylthiol-PEG-(*N*-butyl)acetamide (APB) (Figure 1). HS-ethyl-PEG_{2000} with a molecular weight of ∼2000 g/mol is a commonly used hydrophilic stealth coating for Au nanoparticles. The HS-alkyl-PEG-(N-functionalized)acetamide ligands contain an alkyl spacer connected to the thiol groups that ensures better packing of the following PEG segments on the metal surface, and the PEG segments reduce unspecific interactions. In APG, the PEG segments are terminated with a glucose end group bonded via acetamide, which adds cell-targeting properties. In APB, the PEG segments in the otherwise same ligand are terminated with an *n*-butyl end group bonded via acetamide, displaying a more hydrophobic terminal group for comparison. The relatively small yet significant change in the end group from APG to APB exemplifies the impact of changes in ligand chemistry. We constructed models with the maximum grafting densities of these ligands to gold nanoparticles of approximately 20 nm size consistent with previous experiments. These common grafting densities are 1.5 chains per nm^2 for HS-ethyl-PEG_{2000} due to the steric demand and hydration of PEG[58,59] and 4.2 chains per nm^2 for APB and APG.[55,56]

https://doi.org/10.1021/acsnano.1c08695
ACS Nano 2022, 16, 8766−8783

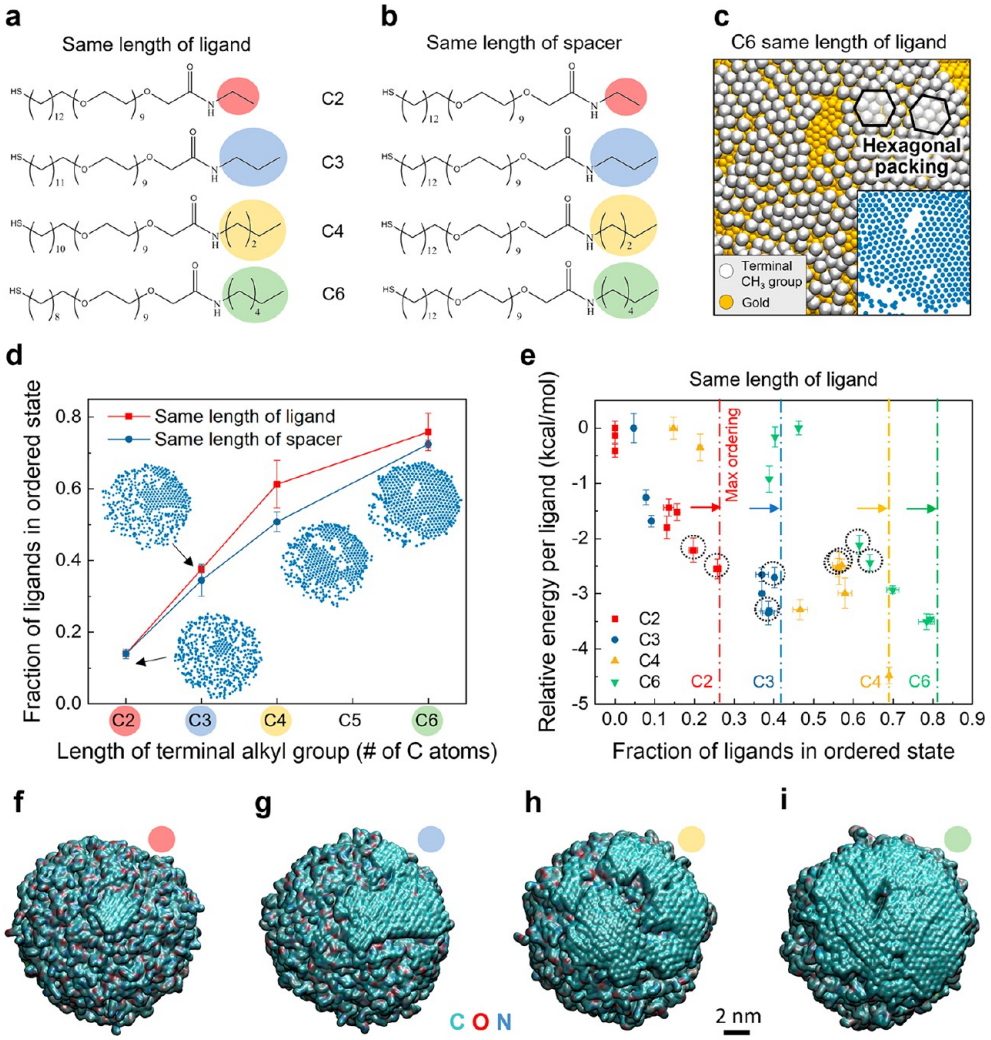

Figure 2. Ligand ordering on 20 nm diameter gold nanoparticles as a function of the length of terminal *N*-alkyl groups in Au-thioalkyl-PEG-(*N*-alkyl)acetamides at 298 K. The grafting density corresponds to the maximum coverage of 4.2 ligands per nm^2 according to experimental data (refs 56 and 57). (a) Composition of a series of ligands of the same length (same overall number of carbon atoms) with N-termination from C2 to C6. The number of carbon atoms in the thioalkyl spacer was adjusted relative to the terminal group. (b) Composition of a series of ligands with the same thioalkyl spacer and variable N-termination from C2 to C6. (c) Positions of terminal methyl groups in C6 ligands relative to the gold nanoparticle surface show hexagonal packing of alkyl chains. The inset highlights average equilibrium positions of carbon atoms in the terminal CH_3 group over 3 ns of simulation time. (d) Fraction of ligands on the nanoparticle surface that assumes an ordered conformation is shown as a function of the length of the terminal alkyl groups. Increasing length increases the degree of order. The images in the chart area show the average equilibrium position of terminal carbon atoms over 3 ns of simulation time. (e) Average total energy of multiple replicas of each model system (C2, C3, C4, C6) relative to the most unfavorable value (=considered equal to zero) as a function of the fraction of ligands in an ordered state. The energies indicate the degree of stabilization and are normalized per ligand for ease of comparison. The fraction of ligands in the ordered state represents the transition from disorder (0.0) toward order (e.g., 0.7). Black circles highlight replicas that started with significantly higher order and decreased in order toward equilibrium. (f–i) Space-filling view of the ligand surfaces on a sliver of gold nanoparticles for *N*-ethyl-, *N*-propyl-, *N*-butyl-, and *N*-hexyl-terminated ligands, respectively.

Differences were noticed in the structure of the ligands, particularly in the amount of surface order and surface roughness (Figure 1a–f). HS-ethyl-PEG$_{2000}$ displays a disordered surface structure with ligands in liquid-like conformations throughout the length of the simulation time (Figure 1a). The disordered structure is consistent with previous experimental and computational observations of disordered PEG coatings at low packing density.[14,61] Irregular conformations of PEG are related to the stereoelectronic preference of the main chain for gauche conformations (O–C–C–O dihedral angles).[62] The terminal methyl groups of the PEG chains exhibit significant mobility and disorder in average positions during the final 3 ns of the simulations, measured by high root-mean-square fluctuations of 6 Å (Figure 1d and Figure S1 in the Supporting Information). Loose packing of the PEG chains and continuous motion with large amplitude allows water molecules to penetrate the ligand layer deeply and evenly up to direct contact with the Au nanoparticle surface (Figure 1g).

HS-alkyl-PEG-(*N*-glucosyl)acetamide and HS-alkyl-PEG-(*N*-butyl)acetamide, in contrast, have rather different dynamics from HS-ethyl-PEG$_{2000}$ and display large barriers to water penetration (Figure 1b,c,e,f,h,i). APG creates a diffuse ligand–water interface whereby many OH groups in the terminal *N*-glucosyl segment interact with the solution phase and are available for interaction with biological media (Figure 1b). The

https://doi.org/10.1021/acsnano.1c08695
ACS Nano 2022, 16, 8766–8783

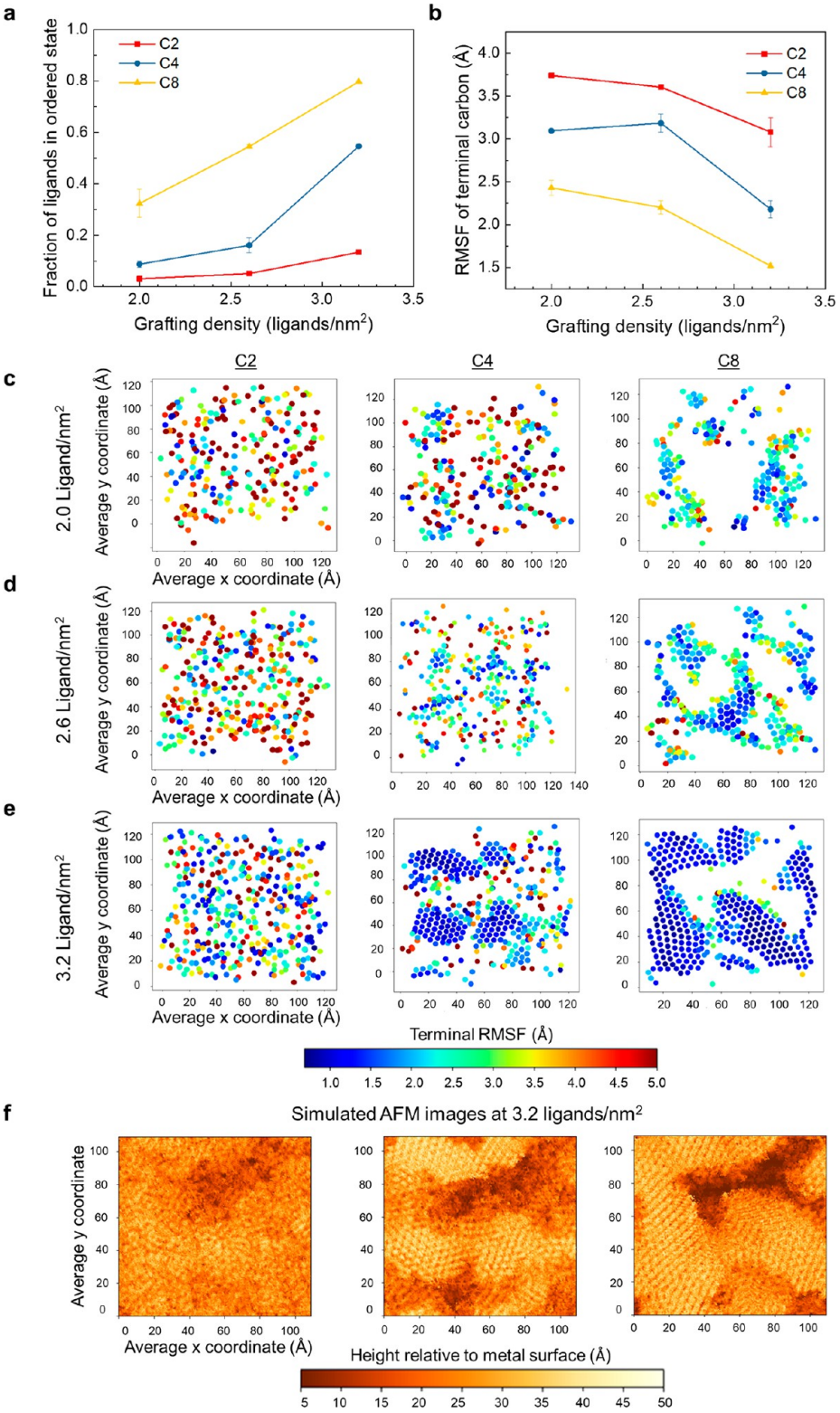

Figure 3. Order versus disorder of thiolalkyl-PEG-acetamide-*N*-alkyl ligands on flat Au(111) surfaces as a function of the grafting density and length of terminal alkyl groups. The grafting density was between 2.0 and 3.2 ligands per nm^2, which corresponds to between 62 and 100% of the maximum grafting density in experiments.[60] (a) Fraction of ligands on the surface in an ordered state. (b) Mobility of the terminal CH_3 groups of different ligands as a function of grafting density, measured by the root-mean-square fluctuation of the equilibrium coordinates. Error bars indicate uncertainties. (c–e) Average (x, y) coordinates of the terminal carbon atoms for (c) C2-, (d) C4-, (e) and C8-terminated ligands, colored as a function of the root-mean-square fluctuation. As ligands assume order and a semicrystalline state, the root-mean-square fluctuation of the position of the terminal CH_3 groups (central carbon atoms) decreases. (f) Computed AFM images of the C2, C4, and C8 ligand coatings at a grafting density of 3.2 ligands/nm^2. The simulation captures height differences of the soft nanostructures of several nanometers in more detail than current AFM or STM instruments.

https://doi.org/10.1021/acsnano.1c08695
ACS Nano 2022, 16, 8766–8783

average position of the amide nitrogen atom in APG ligands shows very limited order (Figure 1e). The density profile of the PEG segments as a function of distance shows that the PEG density gradually decreases as the ligands extend radially from the NP surface, consistent with a loose, disordered structure at the ligand−water interface (Figure 1h). Switching from *N*-glucosyl to *N*-butyl termination resulted in another major change in ligand structure and dynamics (Figure 1c). The APB ligands behave largely like coatings composed of alkyl chains. Many APB ligands formed ordered domains with a distinctive hexagonal pattern of alkyl chains at the ligand−water interface, as characterized by the average position of terminal methyl groups (Figure 1f). The ordered domains exhibit limited mobility of terminal methyl groups and little water penetration (Figure 1i). Unlike the homogeneous surface pattern of HS-alkyl-PEG-(*N*-glucosyl)acetamide and HS-ethyl-PEG_{2000} coatings (Figure 1a,b,d,e), the assembly of the APB ligands was inhomogeneous, and disordered domains formed alongside ordered domains (Figure 1c,f). Ligands in the disordered domains had higher mobility and created a rougher interface with water of exposed CH_3, alkoxy, and CONH groups in comparison to smoother CH_3-terminated surfaces in the ordered domains. The penetration of solvent molecules into the ligand shell correlates with solubility and can serve as a proxy for the interactions with drugs and other small molecules in ligand-modified NPs for therapeutic purposes.

Effect of the Length of Terminal Alkyl Groups on Ligand Order. These initial findings prompted us to study two series of HS-alkyl-PEG-(*N*-alkyl)acetamide ligands (Figure 1c,f,i) on gold nanoparticles to examine the controllability and sensitivity of ligand order versus disorder as a function of the length of the *N*-alkyl end groups (Figure 2). The length was varied from C2 to C6 by attaching ethyl (C2), propyl (C3), butyl (C4), or hexyl (C6) groups to the outer N-terminal end of the acetamide segment. In one series, we held constant the overall length of the ligands, allowing adjustments in the length of the nanoparticle-facing alkyl thiol spacer between C_8 and C_{12} (Figure 2a). In the second series, we held constant the length of the nanoparticle-facing alkyl spacer at C12 and allowed the total length of the ligands to vary (Figure 2b). Across both series of ligands, an increase in the length of the N-terminal alkyl chains from two to six carbon atoms steadily increased the fraction of ligands that assumed an ordered state on the sliver of the gold nanoparticle surface (Figure 2c,d). For an ethyl terminal group, ∼14% of ligands were in an ordered stated state with regular packing and found in small, distributed pockets across the surface (Figure 2d,f). For propyl and butyl terminal groups, approximately 35 and 55% of the ligands were ordered in extended domains, respectively (Figure 2d,g,h). For a longer hexyl terminal group, we found ∼75% of ligands on the surface in an ordered state, mainly within one large cluster (Figure 2d,i). Hereby, the two series of ligands exhibit nearly identical trends (Figure 2d). A slightly larger increase in the order of terminal alkyl chains was observed for the series of ligands with constant total chain length (Figure 2a,d) in comparison to the series with constant spacer length (Figure 2b,d), which can be attributed to the shorter overall ligand length and reduced free volume at the chain ends.

To test whether the initial degree of order of the ligands in the simulation impacts the degree of order in equilibrium, three ligand−nanoparticle conformations with different initial degrees of order for each of the C2, C3, C4, and C6 ligands were subjected to MD simulation in duplicate or triplicate, equal to 8 independent simulations for each terminal group at 298 K (Figure 2e and Figure S2 in the Supporting Information). The stabilization energies per ligand as a function of order show that structures of higher order are consistently more favorable than those with lower order up to a certain length-specific limit (vertical dashed lines in Figure 2e). The trend toward favorable energies and enthalpies in the ordered state is the same regardless of the length of the alkyl tails. In contrast, models that were initially designed with near 100% order lost regularity during equilibration and approached a value of typical order, demonstrating that there is a favorable degree of order characteristic for the length of the terminal alkyl group (data marked with black circles in Figure 2d,e). Therefore, it appears feasible to control the relative amount of disordered and ordered phases by choosing a specific length of the end groups. The simulations also indicate that ligands may become kinetically trapped in energetically less favored disordered structures. These structures have somewhat increased disorder and could be favored by entropy contributions which are more challenging to quantify in molecular simulations.

The large differences in the distribution of terminal groups and in the degree of order are qualitatively consistent with known relations of the ligand structure to the grafting density and temperature,[27,63−65] as well as with the ligand hydrophilicity which has been less explored to date. End groups are a highly sensitive, tunable design parameter that can control the amount of each phase present and expose different segments to the solution phase.

Effect of the Grafting Density of the Ligands and the Length of Terminal Alkyl Groups on the Order on Flat Gold Surfaces. Self-assembled thiol monolayers of uniform chemistry have been studied on gold surfaces for decades,[2,30,66,67] and changes in the grafting density are known to modify conformations, dynamics, and surface patterns.[2,22,30,68,69] In contrast, multisegment ligands as well as precise control of sub-monolayer coverage have not been studied in experiments or simulations to date. Therefore, we examined the effect of the grafting density of HS-alkyl-PEG-(*N*-alkyl)acetamide ligands and of the length of the N-terminal alkyl groups on the formation of patterns and their stability on planar Au(111) model surfaces (Figure 3). We compared SAMs of ligands with *N*-ethyl (C2), *N*-butyl (C4), and *N*-octyl (C8) termination and the same overall chain length (Figure 2a) in the presence of physiological saline solution. The Au(111) surfaces had a 10.9 × 10.9 nm^2 area and had grafting densities of 2.0, 2.6, and 3.2 ligands per nm^2, which represent 62, 81, and 100% of the experimentally measured maximum grafting density on flat gold surfaces for similar hydrated, somewhat bulky ligands.[60] This maximum grafting density of the ligands is lower than that on curved gold nanoparticles (Figures 1 and 2), where the packing density decreases with increasing radial distance from the surface.[2,63] Simulations at full and partial grafting density on flat surfaces may therefore give some insight into how ligands organize on the outside of curved nanoparticle surfaces, help in understanding mechanisms of phase separation, and stimulate future studies. The maximum grafting density is always lower than that of *n*-alkanethiols on gold, which is limited by the cross-sectional area of *n*-alkyl chains of 0.19 nm^2 and amounts to ∼5.2 ligands/nm^2.[2,63,70] Hereby, the long HS-alkyl-PEG multiblock ligands occupy more cross-sectional area to accommodate helical conformations of PEG and solvent penetration.

https://doi.org/10.1021/acsnano.1c08695
ACS Nano 2022, 16, 8766−8783

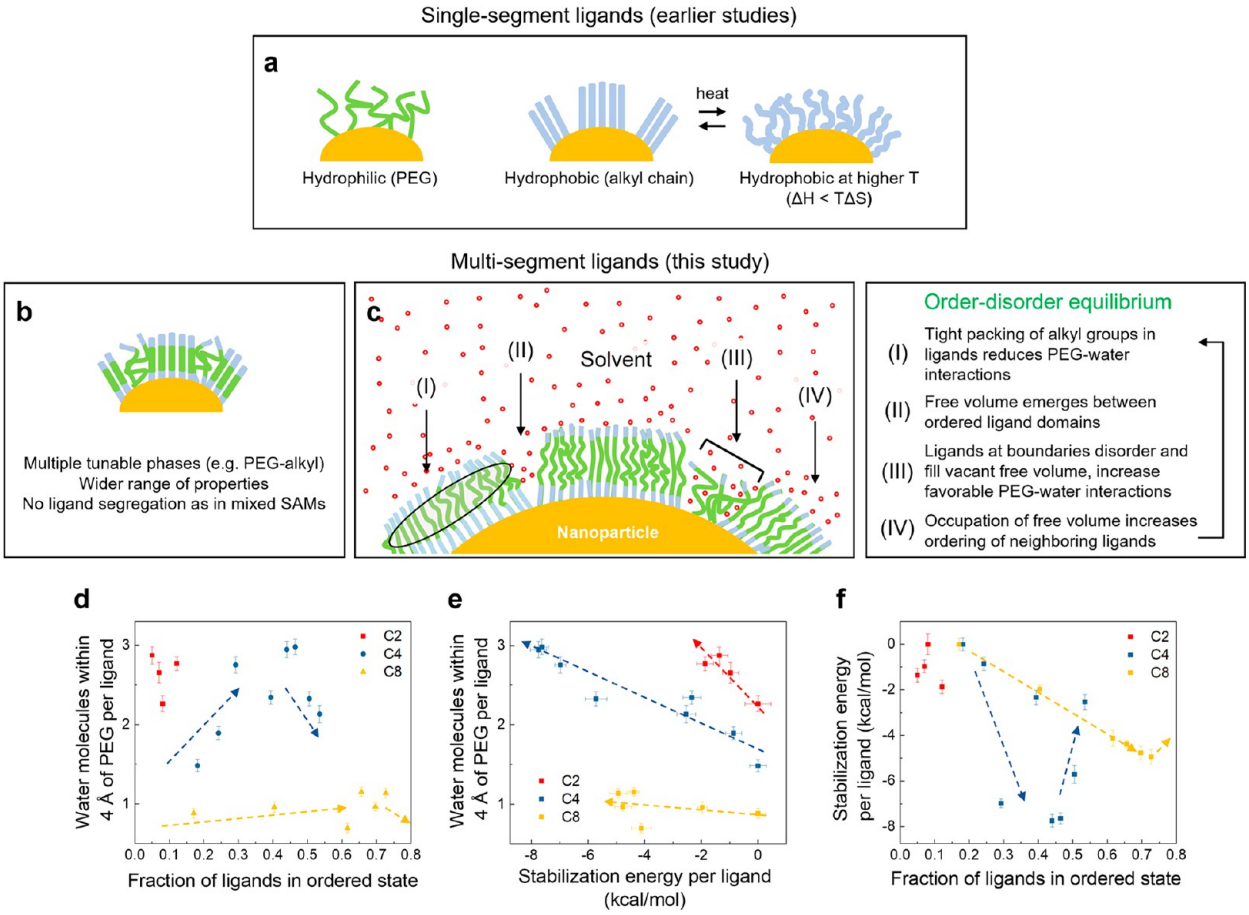

Figure 4. Driving forces for equilibrium patterns of single-segment and multisegment ligands on curved and flat surfaces. PEG−water interactions, van der Waals interactions between alkyl groups, and stabilization energies per ligand are indicated. (a) Previous studies have examined hydrophilic ligand coatings such as PEG, which assumes evenly distributed, disordered conformations on nanoparticle surfaces. Hydrophobic ligands such as alkanethiols form heterogeneously distributed domains of ordered alkyl groups, which can reversibly transition into uniform, liquid-like structures at higher temperature.[2,63] (b) In this work, we examine the structure and dynamics of self-assembled monolayers of multisegment ligands, which display multiple, chemically distinct phases depending on composition. (c) Proposed driving forces for the formation of ordered versus disordered domains and tunable equilibrium structures. (d) Relationship between ligand order and number of water molecules in contact with PEG (within 4 Å). C2 ligands are disordered and allow water penetration. C4-terminated ligands display a peak in PEG−water interactions at 40−45% order. C8-terminated ligands exhibit only minor PEG−water interactions for various degrees of order and assume ∼70% order. (e) Relationship between the number of water molecules in contact with PEG and the ligand stabilization energy (=total average energy per ligand for multiple replicas with different degree of order, whereby the energy of the least preferred replica is set equal to zero; see also Figure 2e). Ligand stabilization increases with a higher number of PEG−water contacts. The correlation is strongest for C2-terminated ligands due to high water penetration and minor alkyl−alkyl interactions and weakest for C8-terminated ligands due to low water penetration and strong alkyl−alkyl interactions. (f) Relationship between ligand order and the relative stabilization energy. The stabilization energy reaches a minimum near the preferred degree of order for each ligand. Data in (d−f) are based on MD simulations of C2-, C4-, and C8-terminated ligands on a flat Au(111) surface with a 5.19 × 5.99 nm^2 surface area.

As the ligand density increases from 62 to 100% of the maximum grafting density, the fraction of ligands in the organized state increases (Figure 3a), and the root-mean-square fluctuation of the position of the carbon atom in the terminal methyl group decreases (Figure 3b). Visually, C4 and C8 ligands increase in order toward higher grafting density, while C2 ligands remain essentially disordered in all instances (Figure 3c−e). The models on the flat Au(111) surfaces also corroborate the relationship between the length of the terminal alkyl groups and ligand order on nanoparticle segments (Figure 2d,e) for multiple grafting densities (Figure 3a,b). At a given grafting density, longer N-terminal alkyl groups increase the fraction of ligands in the ordered state (Figure 3a) and decrease the mobility of the outer methyl groups (Figure 3b).

Ordered ligand domains were visually identified by tight hexagonal packing of the terminal carbon atoms (in terminal CH_3) and by a low root-mean-square fluctuation of their coordinates in equilibrium (<2 Å) (Figure 3c−e). The structural organization of ligands at various grafting densities matches well with the ligand assembly at high coverage on curved NP surfaces (Figure 1c,f). The data show that organization into two phases occurs on both curved and noncurved surfaces. Two-phase organization is highly dependent on the grafting density of ligands and on the length of the N-terminal alkyl groups, which alters the overall ligand hydrophobicity.

Hereby, the simulations reach high resolution on the order of 1−5 pm that is difficult to achieve in experiments. Imaging of soft matter by scanning tunneling microscopy (STM) and in situ atomic force microscopy (AFM) can typically resolve

https://doi.org/10.1021/acsnano.1c08695
ACS Nano 2022, 16, 8766−8783

features in the 100−500 pm range and has limitations to recognize specific functional groups.[66,71] We visualized the resulting surface topography at 3.2 ligands/nm^2 in the form of computed AFM images using the average height profiles from MD simulations (Figure 3f). Currently, it is difficult in AFM and STM experiments to resolve height profiles across several nanometers in the liquid phase.[71] The computational data indicate a larger height for ordered ligand domains up to ∼4.5 nm, while the disordered domains are of lower height, often below 2 nm (Figure 3f). In the ordered systems C4 and C8, bare gold remains accessible between the packed ligand structures. The SAMs show a high sensitivity to the grafting density and length of the terminal alkyl group, which can be combined to control the degree of ligand order and segment availability on the NP surface. The ratio of ordered to disordered regions could be verified using future AFM data.

Driving Forces for Phase Separation and Equilibrium Degree of Order. Earlier studies have shown that ligand coatings take on either evenly distributed structures with homogeneous, disordered ligand coverage such as in PEG-type coatings (Figure 4a, left)[65] or asymmetrically distributed structures with islands or otherwise segregated coverage such as in alkyl thiol-type coatings (Figure 4a, right).[23,24,30] Recent studies still focus on the separation of classical alkyl thiols into chemically uniform ordered and disordered regions at low coverage.[72] In comparison, the two-segment ligands analyzed in this work exhibit different dynamics and can form two chemically separate surface phases using a single ligand type (Figure 4b). In the following, we rationalize the driving forces for the assembly and equilibrium structure of tunable NP-S-alkyl-PEG-(*N*-alkyl)amide ligands based on the observations from molecular dynamics simulation and previous knowledge (Figure 4c).[2] Key contributions arise from PEG and alkyl segments, as well as free volume and solvent (water), which is essential under physiological conditions (Figure 4d−f).

PEG segments take on disordered helical conformations due to the gauche effect, favorable solvent interactions through hydrogen bonds, and configurational entropy.[61,73] These conformations lead to low maximum grafting densities of 1−2 ligands per nm^2 for long, pure PEG ligands (N = 20−100) in experiments (Figure 1).[58,59] The addition of terminal alkyl segments increases orderly ligand−ligand interactions through van der Waals forces, decreases the hydrophilicity of the inner PEG segments, and reduces ligand−water interactions (Figure 4c,I).[2,63] The ligands begin to "separate" out of solution and form ordered assemblies similar to alkanethiols as the energy gain from ligand−ligand ordering largely outweighs PEG−water interactions (Figure 4c,I). The maximum grafting density observed in experiments accordingly increases, depending on curvature, to between 3 and 4.5 ligands per nm^2.[56,57,60] As the ligands assume alkyl block characteristics, they occupy less volume than in the disordered state and open void spaces (Figure 4c,II). The free volume allows adjacent ligands to give up order and reoccupy the vacated free volume (Figure 4c,III). As the number of PEG−water contacts increases, free volume is occupied and more ligands begin to reorder (Figure 4c,IV). In this manner, an equilibrium degree of ligand order is reached that is characterized by a specific number of PEG−water interactions versus a specific number of alkyl−alkyl interactions (Figures 2, 3, and 4b−f).

As an example, PEG−water interactions are the principal driving force for conformations of ligands with short hydrophobic alkyl chains such as C2 (Figure 4d,e). The degree of order is limited to ∼10% because the alkyl chains are too short for significant van der Waals interactions. The degree of order of C4 ligands increases until approximately 40% and decreases from higher order to optimize PEG−water interactions (Figure 4d,e). Stabilization of these structures is balanced by alkyl−alkyl interactions and significant PEG−water interactions. C8 ligands prefer about 70% order due to predominant van der Waals interactions between the longer alkyl chains and have a lower optimum number of PEG−water interactions (Figure 4d,e). Higher order toward 100% would reduce PEG−water contacts.

We find a clear correlation between the number of PEG−water contacts and the overall stabilization of ligand structures, measured by the relative energy per ligand (Figure 4e). Stronger interchain interactions for C8-terminated ligands and decreased importance of PEG-solvent interactions also result in higher order at lower grafting density compared to ligands with shorter terminal alkyl groups (Figure 3a). As the length of the hydrophobic end group increases, the ability of water to reach the PEG segment is reduced due to spatial confinement, seen by the near-constant number of PEG−water contacts for C8 ligands as a function of ligand order on a flat Au(111) surface (Figure 4d,e). The total stabilization energies of the ligands, given relative to the least favorable configuration for each terminal group, quantify contributions by van der Waals interactions between alkyl chains and hydration energies of PEG segments (Figure 4e,f). The trends indicate minima for a favorable fraction of ligand order that balances the two contributions (Figure 4f).

In addition to the length of PEG segments and terminal alkyl groups, surface curvature, grafting density, and the total length of the ligands are expected to influence the formation of ordered and disordered phases. These parameters modify the amount of free volume per ligand and the ability of water to penetrate the ligand layer. For example, ordering of ligands into two phases would occur for lower grafting densities on flat surfaces than on nanoparticles because the packing density of the ligands on nanoparticles decreases as a function of radial distance from the inner surface.[2,63] Entropy contributions also participate in the process, however, they are more difficult to quantify than energy contributions due to the presence of PEG, water, and alkyl chains (see examples of approximate entropy descriptions in ref 74).

The nanopatterned structures of multisegment amphiphilic ligands in the simulation are similar to those observed for chemically different, immiscible cografted ligands ("mixed SAMs") in previous experiments.[36,48,75] In both cases, the ligands form distinct phases for given ratios of hydrophilic to hydrophobic blocks or ligands, respectively. The multisegment ligands hereby have an all-in-one chemistry that prevents segregation of different ligand types on the nanoparticle surface[46,45] and allows improvements in stability[47,48] and access to a wide range of phases with tunable properties. In addition to PEG and alkyl segments, other hydrophilic and hydrophobic segments can be explored, for example, by replacing PEG with polyethers, polyimines, or charged polymers, as well as by replacing alkyl groups with fluorocarbon groups, polydimethylsiloxyl groups, or cell-targeting groups.

Effect of Ligand Conformation on Hydration Energies and Solubility of the Nanoparticles. We analyzed ligand conformations and ligand−solution interactions for different ratios of ordered to disordered domains using visual analysis,

https://doi.org/10.1021/acsnano.1c08695
ACS Nano 2022, 16, 8766−8783

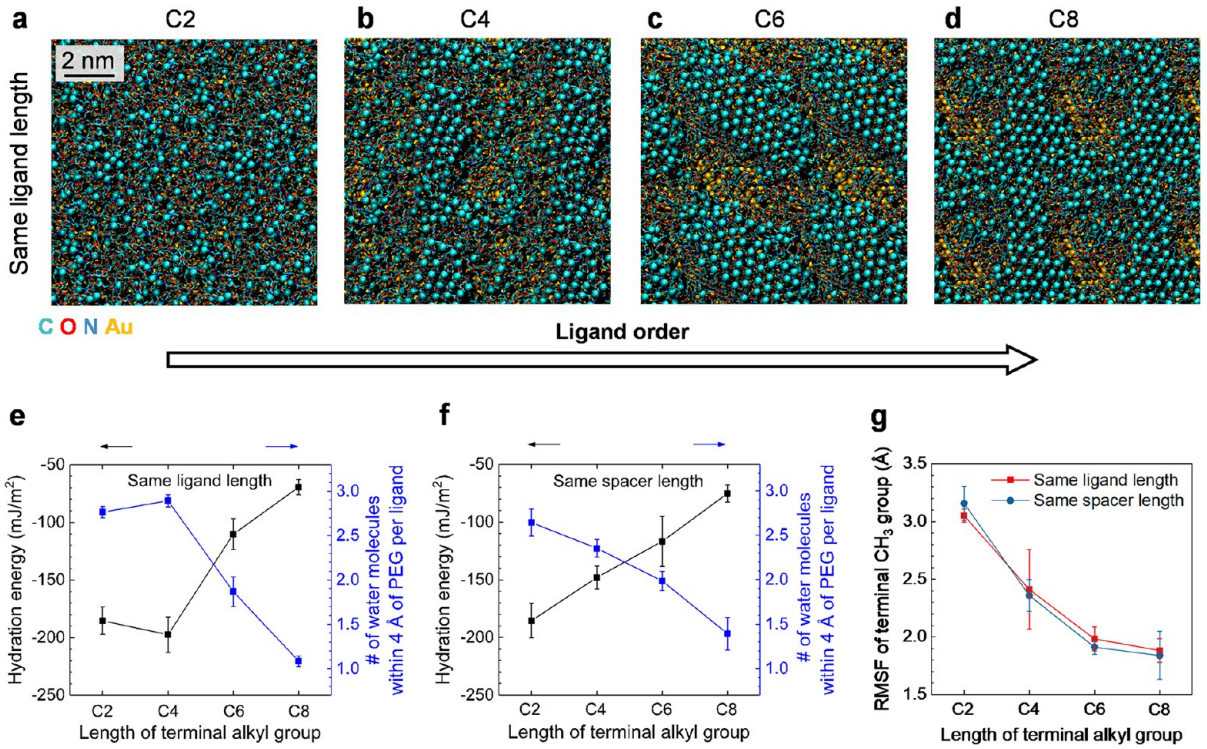

Figure 5. Change in surface properties of ligand-modified flat Au(111) surfaces as a function of the length of the terminal alkyl chain. The models include thiolalkyl-PEG-(*N*-alkyl)acetamide ligands of different *N*-alkyl terminal length at a maximum grafting density of ~3.2 chains per nm².[60] (a–d) Equilibrium snapshots of ligand surfaces with C2, C4, C6, and C8 termination from molecular dynamics simulation in aqueous solution. Ligand backbones are shown in stick display style and carbon atoms in the terminal methyl groups in van der Waals display style to visualize order atop the Au surface. The degree of order of the terminal ligand segments increases from C2 to C8. (e) Hydration energy (left axis), normalized per surface area of gold, and number of water molecules interacting with inner PEG segments. Ligands have the same total length and same number of carbon atoms in this series (see Figure 2a). (f) Hydration energy and number of water molecules interacting with inner PEG segments. Ligands have the same spacer length/increasing total number of carbon atoms in this series (see Figure 2b). Hydration is exothermic in all cases and more favorable for C2 termination compared to C6 and C8 termination (e,f). The hydration energy correlates directly with the number of water molecules able to penetrate and interact with PEG segments (right axes in e,f). (g) Root-mean-square fluctuation of the position of the terminal methyl group in the nanoparticle–ligand model structures. The root-mean-square fluctuation decreases for longer terminal alkyl chains due to increased surface order.

hydration energies, and root-mean-square fluctuations of the position of terminal methyl groups (Figure 5). Ligand models included C2, C4, C6, and C8 termination on flat Au(111) surfaces (5.2 × 6 nm²) at a grafting density of 3.2 ligands per nm² in water.

The conformational order steadily increases for longer terminal alkyl groups (Figure 5a–d). The associated hydration energies are a measure for solubility, i.e., for the formation of stable colloidal solutions, and very favorable for the C2 ligand model at −185 ± 10 mJ/m². Hydration energies show a marked increase to less negative values as the length of the terminal alkyl group increases to C8 up to −70 ± 6 mJ/m²; i.e., hydration becomes less favorable (Figure 5e). This trend is paired with a decrease in the average number of water–PEG contacts. Nevertheless, the negative hydration energies remain significant and comparable to the surface tension of water (72 mJ/m²), even for C8 ligands, in support of solubility (Figure 5e). Similar increases in ligand order and hydration energy for increasing length of the terminal alkyl chain were also found in the series of ligands with constant length of the alkyl spacer (Figure 5f and Figure S3 in the Supporting Information). The simulation results are supported by experiments that demonstrate good solubility for SAMs of C4 ligands[9] as well as solubility for SAMs of C8 ligands, in which case the chemical environment such as cosurfactants also begins to play a role.[76]

Additionally, we tracked the root-mean-square fluctuation of the position of the C atom in the terminal methyl group of the ligands as a measure of ligand mobility, which was earlier proposed to cause loss of ligand entropy upon protein binding and diminish protein adsorption (Figure 5g).[77,78] The root-mean-square fluctuation of the coordinate of the terminal CH_3 group decreases significantly from around 3.1 to 1.8 Å as ligands begin to order with increased length of the N-terminal alkyl chain. The mobility eventually levels out for C8 terminal groups as order reaches a maximum on the flat Au surfaces (Figure 5g). The large changes in hydration energy and in surface structure have the potential to alter nanoparticle aggregation and protein interactions in solution. Aqueous interfacial properties and solubility may be further influenced by the curvature of NPs, and therefore by the particle size distribution. Nanoparticle curvature as well as ligand segment chemistry and ligand length also affects the packing density, effective free volume, and order of the ligands as a function of radial distance[2] with impacts on hydration energies and colloidal stability.

Influence of Solvent Polarity on Ligand Conformation. We then tested the influence of solvent polarity on ligand conformations using MD simulations in water and in

https://doi.org/10.1021/acsnano.1c08695
ACS Nano 2022, 16, 8766–8783

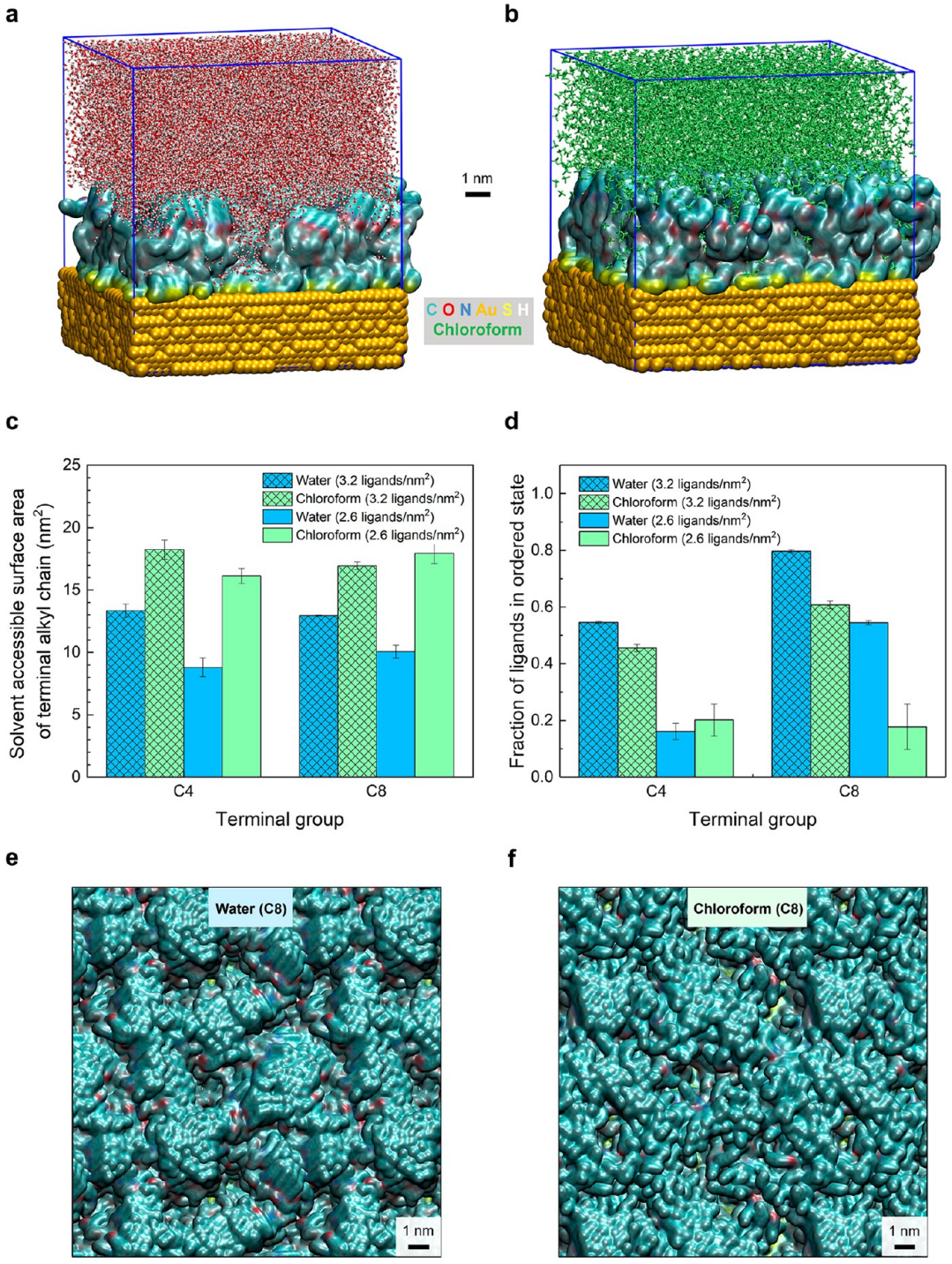

Figure 6. Visualization of thiolalkyl-PEG-(*N*-alkyl)acetamide ligands on flat gold (111) surfaces in aqueous saline solution and in chloroform. The solvent-accessible surface area and degree of ligand order for C4 and C8 terminal alkyl chains are shown at grafting densities of 3.2 and 2.6 ligands/nm^2.[60] (a) Snapshots of Au(111) surfaces of 10.9 × 10.9 nm^2 area coated with thiolalkyl-PEG-(*N*-octyl)acetamide (C8) ligands grafted at 2.6 ligands/nm^2 in salt water (130 mM). (b) Snapshot of the same system in chloroform. (c) Solvent-accessible surface area of the terminal alkyl groups increases drastically from water to chloroform in all models, indicating significant alkyl−chloroform interactions and ligand rearrangement. (d) Fraction of ligands in the ordered state. The degree of order in the terminal alkyl chain decreases in chloroform compared to water due to more favorable interaction with $CHCl_3$. (e) Top view of the C8 ligand surface at a grafting density of 2.6 ligands/nm^2 in aqueous saline solution. C8 ligands form clusters of ordered regions to decrease alkyl−water interactions as well as pockets next to ordered regions to increase water−PEG interactions. (f) Top view of the C8 ligand surface at 2.6 ligands/nm^2 in chloroform. More fluid-like conformations and less ligand order are found compared to water in (e).

chloroform (Figure 6a,b). We utilized flat Au(111) surfaces (10.9 × 10.9 nm^2) with C4 and C8 ligands and two different grafting densities. In chloroform, both C4 and C8 ligands show a marked 30−80% increase in solvent-accessible surface area (SASA) of the terminal alkyl groups (Figure 6c). This trend occurred at both grafting densities of 2.6 and 3.2 alkyl-PEG-

https://doi.org/10.1021/acsnano.1c08695
ACS Nano 2022, 16, 8766−8783

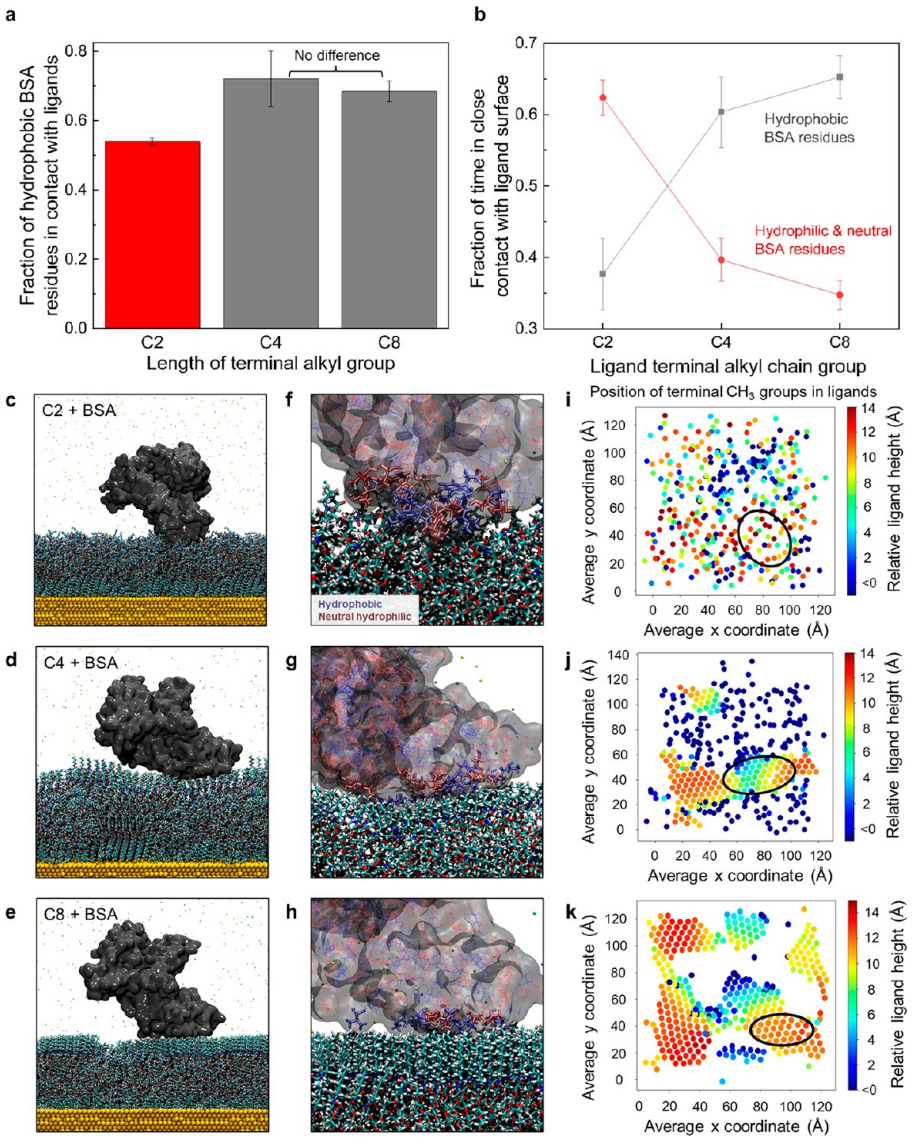

Figure 7. BSA interactions with SH-alkyl-PEG-(*N*-alkyl)acetamide ligand coatings at 3.2 ligands/nm^2 (ref 60) and C2, C4, and C8 terminal chain lengths. (a) Fraction of hydrophobic BSA residues in contact with ligands on the nanoparticles, in relation to all bound residues. Contact was defined as <3 Å distance of protein atoms from any ligand atom. (b) Fraction of time of close contact of hydrophobic and other BSA residues with the ligand surface. (c–e) Snapshots of BSA interacting with C2-, C4-, and C8-terminated ligand surfaces. (f–h) Close-up images of BSA interacting with thiol-PEG-(*N*-ethyl)acetamide (f), thiol-PEG-(*N*-butyl)acetamide (g), and thiol-PEG-(*N*-octyl)acetamide (h). Hydrophobic residues are colored blue, and hydrophilic residues are red. BSA flattens when binding to ordered, hydrophobic surfaces (g,h), and the fraction of hydrophobic contact residues increases. (i–k) Average *x*, *y*, and relative *z* coordinates of the carbon atoms in the terminal CH_3 groups of the ligands. BSA binding positions are encircled. Ligands with the terminal C4 alkyl group display a rougher surface than ligands with the terminal C8 alkyl group.

thiol ligands per nm^2. Lower grafting density led to larger increases in SASA. Concomitantly, the fraction of C4 and C8 ligands in the ordered state decreased in chloroform relative to water or stayed the same in the case of C4 ligands at a low grafting density of 2.6 ligands/nm^2 due to low initial order (Figure 6d). Accordingly, an increase in SASA in $CHCl_3$ strongly correlates with a decrease in ligand order, except when the fraction of ligands in the ordered state in water was low to begin with (<0.20). The difference in ligand order is visualized in the top view of C8 ligands, which shows ordered domains in water (Figure 6e) and more dispersion and fluidity in $CHCl_3$ (Figure 6f). Low grafting densities of 2.0 ligands/nm^2 lead to high disorder in both solvents and were not further analyzed (see Figure 3a for water).

Functionalizing nanoparticles with ligands to permit nanoparticle dispersion in both aqueous and organic solvents has been of notable interest.[79,80] In experiments, nanoparticles coated with mixtures of ligands similar to C8 and octanethiol were shown to be soluble in both water and chloroform by altering the ratio of the two ligands.[76] The origin of solubility in both solvents was proposed to be related to conformational changes in the alkanethiol-PEG-(*N*-octyl)acetamide (C8) ligands, which can adjust the amount of free volume depending on the relative length of thioalkyl head groups to C8 tail groups, and expose more or less of the middle PEG block.[76] Our simulations and quantitative metrics at the molecular scale demonstrate that coatings with a single type of multisegment ligands can enable similar conformational changes by changing

https://doi.org/10.1021/acsnano.1c08695
ACS Nano 2022, 16, 8766–8783

the ligand free volume, which exposes different ratios of PEG and hydrocarbon to the solvent phase. Multisegment ligands such as thioalkyl-PEG-(*N*-alkyl)amides may thus disperse nanoparticles in polar and nonpolar solvents without requiring mixtures of chemically different ligands. Key design parameters are the length of terminal alkyl groups, PEG segments, and the grafting density. Also, factors such as nanoparticle size and ligand length could transform coatings between insoluble and soluble.

Influence of Ligand Chemistry on Protein Interactions. To understand the effect of ligand chemistry on interactions with proteins, we considered BSA as a common example.[81,82] The initial interaction of BSA with thiol-PEG-(*N*-alkyl)amide ligands of C2, C4, and C8 termination on flat Au(111) surfaces was examined at a grafting density of 3.2 ligands/nm^2 in saline solution (130 mM) (Figure 7). We identified bound BSA residues within 0.3 nm distance and contact times with each ligand layer over a simulation time of 125 ns using 15 different start configurations (Figure 7a,b). The simulations showed instances of binding and nonbinding of BSA to the ligand surfaces in support of typical equilibria. Since simulations in all-atom resolution do not allow sampling of the complete conformational space of BSA upon binding, we utilized replicas of nearly identical initial configurations of BSA that lead to binding on each ligand surface. The local binding data are reproducible and enable comparisons of binding as a sole function of different ligand coatings (see Computational Methods). The fraction of bound hydrophobic versus neutral and hydrophilic contact residues of BSA grew from C2 to C8 ligands, related to increasing ligand order. Fifty-four percent of hydrophobic residues among all BSA contact residues were in close contact with C2 ligands, 72% with C4 ligands, and 68% with C8 ligands with uncertainties of 3−5% (Figure 7a). Interestingly, the fraction of hydrophobic contacts was significant even for the relatively hydrophilic C2 ligand surfaces. The fraction of time of BSA residues in closest contact with the ligand coatings consistently showed an increase in the percentage of hydrophobic residues in the same order from 40 to 65% (Figure 7b). The contact time of neutral and hydrophilic residues of BSA diminished accordingly. The data demonstrate changes in the relative importance of the residue types in the protein for binding as a function of ligand ordering and the multisegment composition. The difference in the amount of bound hydrophilic BSA residues relative to hydrophobic residues arises from the more hydrophilic nature of the disordered C2 surface compared to the ordered regions of C4 and C8. The change in preference from hydrophilic to hydrophobic residues as the length of the alkyl tail increases could result in more protein denaturation on ordered ligand surfaces since then hydrophobic regions internal to the protein may experience a stronger driving force to rearrange and display on the protein surface.

These differences in ligand affinity toward specific protein residues also led to visible changes in the shape and orientation of BSA during the initial binding phases (Figure 7c−h). BSA penetrates the ligand−water interface upon binding to the disordered C2-terminated ligand surface and features a higher total number of protein−ligand contacts (Figure 7c,f and Figure S4a,b in the Supporting Information). The surface of BSA then appears somewhat corrugated. During binding to the ordered hydrophobic surfaces of C4-alkyl- and C8-alkyl-terminated ligand surfaces, the protein binding region shows some flattening, indicating the onset of denaturization (Figure 7d,e,g,h). Upon binding to ordered regions of C4 and C8 ligands, differences in the dynamics of closest contacts (Figure 7b) may be associated with the increased surface roughness of C4 compared to C8 (Figure 7i−k). As recently suggested, increased roughness can increase the surface hydrophilicity of ordered alkyl chains.[83]

Further trends can be seen from the interaction energies between BSA and the ligand layers over the final 10 ns of simulation time (Figure S4 in the Supporting Information). Larger fluctuations in interaction energy were observed for ligands with shorter terminal alkyl groups (C2), which indicate less stability of contacts in comparison to C4 and C8 ligands. Previous experimental measurements have suggested a correlation between larger fluctuation and reduced binding stability,[84] which agree with the findings by simulation. We also observed selectivity in binding of hydrophobic versus hydrophilic residues of BSA during the interaction with SH-alkyl-PEG-(*N*-butyl)acetamide ligands versus SH-alkyl-PEG-(*N*-glucosyl)acetamide ligands grafted to curved Au nanoparticle slivers, respectively (Figure S5a,b in the Supporting Information). Additional details are described in section S1 in the Supporting Information.

In summary, BSA interacts with the C2 and C4/C8 ligand coatings using different residues, which strongly suggests that the composition of ligand segments influences the BSA binding process. While simulations cannot resolve protein dynamics over realistic time scales (milliseconds and beyond), modifications in ligand tail chemistry show promise to change preferences toward hydrophilic or hydrophobic residues on proteins and, as a result, impact protein orientation and dynamics during initial adsorption. Different sections of protein surfaces likely have higher affinity toward specific ligand coatings depending on the design toward specific residues, which could inhibit protein active sites once bound to the surface. Nanoparticles for therapeutic use often require retention of the availability of protein active sites to enter cells or pass biological barriers.[85,86] Fine-tuning protein orientation during adsorption is therefore very important and care must be taken that changes in ligand tail chemistry do not alter protein binding in unexpected ways.

CONCLUSION

We analyzed the organization and dynamics of multisegment thiol ligands on metal nanoparticle surfaces in high resolution using all-atom molecular dynamics simulation and observed tunable separation into different phases at common grafting densities. Patterning in the self-assembled monolayers consisting of single-component and multisegment ligands occurs through the simultaneous exposure of various functional groups to the solution interface in controllable ratios. Molecular organization in this interfacial region modulates the interaction with solvents and proteins, offering potentially increased control for diagnostic and therapeutic applications.

Our study overcomes difficulties in quantitative analysis and in situ measurements using current laboratory techniques through accurate all-atom MD simulations with the INTERFACE-CHARMM force field. Specifically, we examined the assembly of HS-ethyl-PEG, HS-alkyl-PEG-(*N*-glucosyl)-acetamide, and HS-alkyl-PEG-(*N*-alkyl)acetamide ligands, which differ in terminal functionality and length of terminal *N*-alkyl groups, on gold nanoparticles and flat gold surfaces. The ratio of ordered to disordered terminal ligand portions could be controlled through changes in the length of the

https://doi.org/10.1021/acsnano.1c08695
ACS Nano 2022, 16, 8766−8783

terminal alkyl groups as well as in grafting density. Increasing length of terminal segments from ethyl to octyl drastically increased the fraction of ordered domains. Phase-separated surface structures resemble phase-separated mixed SAMs composed of hydrophobic and hydrophilic ligands. The analysis of 3D patterns, stabilization energies, solvent penetration, and expected AFM profiles lead to a thermodynamic model to explain and tune the associated properties. We also show preliminary evidence for major differences in protein binding as a function of the ligand surface morphology using BSA.

The driving forces behind phase separation, pattern control, and protein binding involve the confinement of the ligands, their length, enthalpy of ordering, and solvent interactions. Trends in ligand organization and dynamics are similar on curved and flat Au surfaces. Different ratios of ordered to disordered ligands modify the surface mobility, the penetration of water into the ligand layer, and overall hydration energies of the ligand-modified nanoparticles. Longer terminal alkyl chains decrease ligand mobility and increase ordering and hydration energies to smaller negative values. Changing the solvent from saline solution to chloroform causes an increase in solvent-accessible surface area of the terminal alkyl chains and a decrease in ligand order, which could be applied to design nanoparticles for phase transfer between organic and inorganic solvents. Binding of proteins to ordered or disordered regions of the coating alters the ratio of hydrophobic to hydrophilic residues, which may influence protein orientation during initial adsorption onto ligand-coated nanoparticle surfaces and affect protein stability.

The observations also suggest that multisegment ligands of other diverse chemistries could be suitable to form SAMs with surface heterogeneities and tunable phases. The sensitivity of the degree of ligand order to small changes in ligand free volume indicates that coatings on polydisperse nanoparticles could have different properties from one end of the size spectrum to the other. Specifically, hydrophobicity and spatial confinement of SAM surfaces can be controlled by tailoring the grafting density of the ligands, the overall length, as well as the length of the hydrophobic ligand tail. Engineering amphiphilic functions into the ligands likely may allow control over surface patterns and properties of ligand-coated nanoparticles to enhance control of the in vivo fate and selectivity for therapeutic and diagnostic purposes.

The findings also illustrate that in silico studies are helpful to understand pattern formation in SAMs, associated electrolyte interfaces, and origins of differential protein binding. All-atom MD simulations fill gaps in present laboratory instrumentation, especially at the accessible time scale (up to ∼1 μs) and model sizes (up to ∼100 nm) and require careful interpretation for larger scales. Going forward, laboratory and clinical measurements are needed to validate and apply the results. Full characterization of multisegment ligand dynamics and protein interactions on nanoparticles of practically relevant sizes is an exciting area for future work.

COMPUTATIONAL METHODS

Curved Nanoparticle Surfaces and Ligand Coatings. *Model Building.* Models of metal surfaces and ligands were built using the Material Studio graphical user interface.[87] The nanoparticle sliver was created by constructing a 20 nm diameter Au nanoparticle and then cutting out a 13 × 13 nm^2 section of the surface used in the simulations. Ligands were placed equidistant from one another on the Au nanoparticle sliver surface with average maximum grafting densities of about 100%, informed by experimental data. Accordingly, the grafting density was 1.5 ligands/nm^2 for HS-PEG$_{2000}$[58,59] and 4.2 ligands/nm^2 for HS-alkyl-PEG-(*N*-glucosyl)acetamide and HS-alkyl-PEG-(*N*-butyl)acetamide.[56,57] These grafting densities account for the approximate nanoparticle diameter, the presence of alkyl spacers of variable length between the sulfur atom and the PEG atoms, and the tendency of PEG to take on a helical conformation with a larger footprint than alkyl chains. The thiol group was bound to Au using a significant well depth of sulfur of 0.47 kcal/mol in the Lennard-Jones (LJ) potential (along with r_{min} = 4.4 Å), which mimics covalent bonding as utilized in previous simulations of metal−thiolates using IFF.[53,88] The systems were then solvated with approximately 120,000−160,000 TIP3P water molecules in 130 mM NaCl saline solution, containing approximately 300−400 Na^+ and Cl^- ions (Figure 1). All simulation boxes were overall electroneutral, the ligands carried no ionic groups, and the simulations conditions correspond to near-physiological pH values of 7. The results are valid for moderate fluctuations in pH value (±several units).

Models of HS-alkyl-PEG-(*N*-ethyl)acetamide (C2), HS-alkyl-PEG-(*N*-propyl)acetamide (C3), HS-alkyl-PEG-(*N*-butyl)acetamide (C4), and HS-alkyl-PEG-(*N*-hexyl)acetamide (C6) on the nanoparticle sliver were created in the same manner.

Simulation and Analysis. Every system was subjected to eight independent MD simulations to analyze equilibrium structures and dynamics. Steady state was reached after 15−35 ns, followed by data collection during an additional 3 ns period. Among the eight independent runs, three classes of starting conformations were used. Three out of eight of the simulations used an initial, unprocessed start structure built using the Material Studio graphical user interface. Another 3/8 of the simulations used a start structure that was first annealed at 400 K for a duration of 100−300 ps to facilitate partial or full ligand disorder. Annealing was then followed by a MD simulation at 298.15 K. The final 2/8 of the simulations employed an initial structure that was first subjected to MD simulations in vacuum for 100−200 ps prior to solvation and subsequent equilibration in solution. These setups promoted initial ligand ordering. Using a variety of eight start structures enabled unbiased modeling of each ligand type with widely different initial degrees of order (Figure 2).

Addition of Protein (BSA). Configurations of the nanoparticle sliver with ligands in equilibrium configurations were used as initial structures to simulate protein binding (Figure S5 in the Supporting Information). We utilized the initial structure PDB ID 3v03 of BSA in the native state.[89] One molecule of BSA was introduced into the model of the respective ligand−NP structure within a distance of 5 Å from the nearest point of the ligand layer. The protein was placed in two distinct conformations above each ligand-modified nanoparticle, followed by unrestrained MD simulations (Figure S5 in the Supporting Information). Our aim was to probe specific protein−ligand interactions in comparable orientations rather than sampling the full configuration space of protein binding, which is hardly possible.

Flat Au (111) Surfaces and Ligand Coatings. *Model Building.* Slabs of flat Au(111) surfaces were created with a surface area of 10.9 × 10.9 nm^2 as well as 5.19 × 5.99 nm^2, with a thickness of 2.8 and 2.0 nm, respectively. Ligands were introduced on both surfaces by first equilibrating sulfur atoms on the Au surfaces at the chosen grafting density through simulation in vacuum for 1 ns at 298 K. We utilized grafting densities of 2.0, 2.6, and 3.2 ligands/nm^2, which correspond to 62, 81, and 100% of the typical coverage on flat gold surfaces for this type of ligand in experiments.[60] Entire ligands were then placed at the location of the sulfur atoms, and every system was subsequently solvated with TIP3P water, which extended the system size by roughly 6 nm above the height of the ligand layer in the *z* direction (Figures 3, 4, and 5). Models of flat, ligand-coated gold (111) surfaces in chloroform were constructed using the same protocol except that $CHCl_3$ was used for solvation instead of TIP3P water molecules.

Simulation and Analysis. Initial simulation and analysis followed the same protocol as for nanoparticle surfaces. The ligand-functionalized flat Au(111) surfaces of 5.19 × 5.99 nm^2 area were used for

https://doi.org/10.1021/acsnano.1c08695
ACS Nano 2022, 16, 8766−8783

calculations of the hydration energy. The models with C2, C4, C6, and C8 ligands coatings were built and equilibrated both with and without subsequent solvation, as required for the computation of the hydration energy using a three-box method.[90]

Addition of Protein (BSA). Flat Au(111) surfaces of 10.9 × 10.9 nm^2 area with ligands (C2, C4, C8 terminal groups) at a grafting density of 3.2 ligands/nm^2 and lowest energy after equilibration were employed for simulations of the interactions with BSA. Water molecules were removed from the equilibrium models to place a single BSA protein with nearest residues 5 Å away from the ligand-coated Au surfaces. The initial location of the protein in x and y directions was chosen to be nearly identical for the three systems (Figure 7). The models were then solvated in an electrolyte solution of 130 mM NaCl. The addition of ionic species showed negligible effects on ligand organization and dynamics in comparison to models using pure water molecules for solvation. Models of three different protein orientations relative to the surface were constructed for each ligand termination, of which some resulted in binding and some in desorption after 125 ns. Binding configurations were run with multiple replicas and binding data are reported as an average for these simulations.

Simulation Protocol. Molecular dynamics simulations were carried out using the Nanoscale Molecular Dynamics program (NAMD) and the IFF-CHARMM36 force field.[91−93] IFF models for metals and minerals achieve high accuracy and are compatible with biomolecular and organic force fields, including sensitive applications such as in catalysis.[94−97] For the simulation of ligand-modified nanoparticle sections, first, brief energy minimizations of several hundred steps were carried out to reduce atomic close contacts. Then simulations were performed at 298.15 K in the NPT ensemble with the Langevin thermostat and pressure piston to maintain the pressure at 1 atm unless otherwise specified. Models not containing vacuum were first subjected to short simulations in the NVT ensemble (200 ps) followed by production runs in the NPT ensemble. Due to the considerable size of the models containing nanoparticle slivers (400,000−600,000 atoms), a 9 Å LJ cutoff with a switching function to zero energy at 8 Å was applied for LJ interactions. Electrostatic interactions were calculated using the particle-mesh Ewald method (tolerance of 10^{-2}), including a direct summation up to 9 Å distance. The ShakeH algorithm was employed, which uses rigid bonds between hydrogen and their bonded neighbor atoms, allowing a time step of 2 fs compared to a typical time step of 1 fs and access to longer simulation times (Figures 1 and 2). Simulations were carried out for 20−45 ns with analysis performed during the final 3 ns.

Simulations of BSA in contact with the C2-, C4-, and C8-coated flat Au(111) surfaces of 10.9 × 10.9 nm^2 size were also carried out with a 9 Å cutoff and 8 Å switching distance, the ShakeH algorithm and a time step of 2 fs for total simulation times of 110−140 ns (Figure 7). The analysis was carried out for initial BSA configurations that showed significant binding to the three different ligand surfaces. Results are reported as an average over two independent simulation replicas for each ligand. Data on specific interfacial recognition on the local scale are reproducible and have only small uncertainties (error bars in Figure 7a,b). Full sampling of protein−surface binding is computationally not feasible and was not attempted.

On the flat Au(111) surfaces of 10.9 × 10.9 nm^2 area without the presence of BSA, we carried out further MD simulations in high accuracy for comparison, including a 12 Å LJ cutoff, a 10 Å switching distance, a particle-mesh Ewald tolerance of 10^{-6} for Coulomb interactions, and a 1 fs time step. These conditions were used to examine the dynamics of C2, C4, and C8 ligand coatings at grafting densities of 2.0, 2.6, and 3.2 ligands/nm^2 in aqueous solution, as well as at a grafting density of 3.2 ligands/nm^2 in chloroform (Figures 3 and 6). Steady state was indicated by energy fluctuations around a constant average and minimal changes in ligand order after 15−20 ns. The simulations were then extended for a minimum duration of 3 ns for data collection and analysis.

On the flat Au (111) surfaces of 5.19 × 5.99 nm^2 area and ligand assemblies with a grafting density of 3.2 ligands/nm^2, MD simulations reached a steady state after 20−55 ns. The simulations were continued for a minimum of 5 ns to perform analyses, resulting in total simulation times of 25−60 ns. These simulations utilized a 12 Å cutoff and a switching function applied at 10 Å for Lennard-Jones interactions, a Ewald tolerance of 10^{-6} for Coulomb interactions, and a time step of 1 fs. Simulations with each ligand type were repeated in at least three independent MD simulations, and the three simulations of lowest average total energy were used for analysis. Ligand assemblies in vacuum were simulated using the same protocol with simulation times ranging from 25−30 ns (Figures 4 and 5).

Force Field Parameters for Chloroform. Force field parameters for chloroform close to IFF standards were developed starting with the CGenFF36 parameters for trichloroethane, which have critical shortcomings.[98] Atomic charges were modified to align with dipole moments of $CHCl_3$ from experiments and the carbon−chlorine bond length was altered from 1.77 to 1.75 Å to be consistent with experimental data (Table 1).[99] Other parameters were unchanged.

Table 1. Improved Nonbonded Force Field Parameters for Chloroform Used in Molecular Dynamics Simulations[a]

	atomic charge (e)	$R_{min}/2$ (Å)	12-6 LJ well depth, ε (kcal/mol)
C	0.39	2.000	0.0320
Cl	−0.13	1.910	0.3100
H	0	1.340	0.0450

[a]Bonded parameters, except for the C−Cl bond length, were the same as those in CGenFF36.

The improved force field reproduced the experimentally measured dipole moment within 1% (1.04 D experimental, 1.047 computational D), the density within ∼1% (1.478 g/mL experimental, 1.459 g/mL computational), and the vaporization enthalpy within 12.5% (31.3 kJ/mol experimental vs 35.2 kJ/mol computational).[99] The model was sufficient to analyze qualitative and semiquantitative changes in ligand organization on the Au nanoparticle when using $CHCl_3$ as a solvent instead of water. Simulations of the nanoparticle−ligand systems with varied grafting density in $CHCl_3$ followed the same protocol as in aqueous solution with TIP3P water molecules using a 10.9 × 10.9 nm^2 even Au(111) surface (Figure 6).

However, we note remaining inconsistencies in CGenFF even after modifications. For example, the 12−6 Lennard-Jones well depth of hydrogen atoms of 0.045 kcal/mol is much higher than validated values of 0.015 kcal/mol in IFF,[100] and even larger than the well depth of 0.032 kcal/mol of carbon atoms in CGenFF, which are clearly more polarizable than hydrogen atoms (Table 1).[99]

Validation of Accelerated MD Simulations. Due to the large scale and large number of model systems, we accelerated MD simulations to be approximately 3.2 times faster than usual for IFF MD. We employed coarser cutoffs for nonbond interactions, the ShakeH algorithm, and a larger time step (Figure S6 in the Supporting Information). The cutoff for LJ interactions was set to 9 Å with 8 Å distance for force switching, a particle-mesh Ewald tolerance of 10^{-2} was used, and a 2 fs time step was enabled by the ShakeH algorithm. In comparison, the usual high accuracy settings include a 12 Å LJ cutoff, no force switching (or a 10 Å switching distance), particle-mesh Ewald tolerance of 10^{-6}, and a time step of 1 fs.

Simulations of the C2 and C4 ligand coatings on the curved nanoparticle surfaces were carried out using accelerated and high accuracy settings. All ordered conformations were found to be equally favorable, and we observed no significant changes in ligand ordering, dynamics, or other trends. The percentage of ligands in the ordered state increased by less than +4% when high accuracy was applied compared to reduced accuracy (Figure S6a in the Supporting Information). Absolute energies changed as expected, and relative energies per ligand were reasonably close within approximately 0.5 kcal/mol when low accuracy settings were applied (Figure S6b in the Supporting Information). We also tested the dynamics of BSA in solution and found no visible changes in secondary structure or solvent-accessible surface area when high accuracy versus accelerated settings were applied. In summary, the accelerated settings did not

https://doi.org/10.1021/acsnano.1c08695
ACS Nano 2022, 16, 8766−8783

significantly impact the quality of the results. The analysis of ligand-modified nanoparticles and protein binding is feasible using accelerated MD simulations (Figure S6 in the Supporting Information).

Analysis of Ligand Dynamics and Average Density Profiles. The dynamics of the ligand-covered nanoparticles from MD trajectories was visually analyzed using the VMD program.[101] Density profiles of the ligands along the vertical z dimension were calculated in 1 Å resolution along the z coordinate of the system using a 1 × 1 nm^2 square (x by y coordinate) in the center of the Au NP (Figure 1g–i). The solvent-accessible surface area was calculated using a probe of 1.4 Å radius, which is a common value, using the VMD program.

Analysis of Ligand Order. Once simulations of SAMs of HS-alkyl-PEG-(end group) ligands reached equilibrium, the average location of the terminal CH_3 groups of each ligand (or the amide N atom) was recorded as an average over the final 3 ns of simulation time. If a given methyl group had three neighbor methyl groups with an average distance of less than 6 Å and a root-mean-square fluctuation of less than 2.5 Å, it was classified to be in an ordered state (Figure S7 in the Supporting Information). The number of ligands in an ordered state was divided by the total number of ligands on the surface to obtain the fraction of ordered ligands. The fraction of terminal ligand order was calculated from 3 independent simulations. The reported values are an arithmetic average of these three simulations and error bars represent the standard deviation (Figure 2d,e, Figure 3a, and Figure 4d,e).

Computation of AFM Images. The computed AFM images (Figure 3f) were obtained from the average coordinates of 20 frames during the last 200 ps of the simulations. The simulation box was divided into 200 × 200 grid points, and the average height of the topmost atoms of the ligands within each grid point was plotted using a color scale, without distinction of the atomic identity.

Computation of Hydration Energies. Hydration energies were calculated using a three-box method (Figure S8 in the Supporting Information).[90] For each ligand type, at least three independent simulations were carried out for the ligands on the gold surface in water (E_1), the ligands on the gold surface (5.2 × 6 nm^2) in vacuum (E_2), and bulk water using the TIP3P water model (E_3). Average energies were calculated during the equilibrium portions of the trajectories (last 50%). The three simulations with the lowest average energies in solution ($\bar{E}_1$) and in vacuum ($\bar{E}_2$) were then used to calculate the hydration energies:

$$E_{hyd} = \bar{E}_1 - \bar{E}_2 - \bar{E}_3 \quad (1)$$

The results of E_{hyd} were adjusted to represent the hydration energy of the ligand-covered side of the slab assuming the known hydration energy for the bare gold surface of −387 mJ/m^2 on the other side of the slab (Figure S8 in the Supporting Information).[90] As an example, the absolute value of the hydration energy for C2 ligands was −185 mJ/m^2 (Figure 5e,f).

Analysis of Ligand–Protein Contacts. The fraction of hydrophobic and hydrophilic residues of BSA in contact with the ligand surface was analyzed using the selection tool in VMD,[101] which classifies hydrophobic and nonhydrophobic residues. First, the total number of BSA–ligand contacts was recorded for pairwise distances of 3 Å or less between protein atoms and ligand atoms (Figure 7a). Second, the closest contacts between BSA and the ligand surface were recorded as an average over time, i.e., only the smallest pairwise distance in each frame (Figure 7b). The residues were classified as hydrophobic or nonhydrophobic, and the data were averaged over 1000 frames during the final 3 ns in both cases. The analysis was performed only on simulations where BSA remained continuously bound to the ligand surface (two independent simulations for each ligand surface).

ASSOCIATED CONTENT

Supporting Information

The Supporting Information is available free of charge at https://pubs.acs.org/doi/10.1021/acsnano.1c08695.

Equilibrium patterns of terminal functional groups of ligands grafted to a section of a 20 nm diameter Au nanoparticle, examples of initial and equilibrium conformations of ligands on the section of a Au nanoparticle, visualization of conformational changes of thioalkyl-PEG-(*N*-alkyl)acetamide ligands with a constant alkyl spacer length and varied length of the terminal alkyl chain, interactions between BSA and HS-alkyl-PEG-(*N*-alkyl)acetamide ligand coatings, interactions of BSA with thioalkyl-PEG-(*N*-butyl)acetamide and thioalkyl-PEG-(*N*-glucosyl)acetamide ligand coatings on a sliver of a 20 nm diameter gold nanoparticle, comparison of simulation performance with settings of high and reduced accuracy, visualization of the ligand structure on flat Au(111) surfaces, illustration of the three-box method employed to calculate the hydration energy of the ligand coatings with periodic boundary conditions, additional discussion of BSA–ligand interactions (PDF)

Supporting movie file highlighting the formation of different ligand patterns for C2 and C4 termination (MP4)

Supporting data file that includes selected 3D start structures and equilibrated models, simulation scripts, and the IFF-CHARMM36 force field file to reproduce the simulations (ZIP)

AUTHOR INFORMATION

Corresponding Author

Hendrik Heinz − *Department of Chemical and Biological Engineering, University of Colorado Boulder, Boulder, Colorado 80303-0596, United States;* orcid.org/0000-0002-6776-7404; Email: hendrik.heinz@colorado.edu

Authors

Samuel E. Hoff − *Department of Chemical and Biological Engineering, University of Colorado Boulder, Boulder, Colorado 80303-0596, United States*

Desiré Di Silvio − *Soft Matter Nanotechnology Group, CIC biomaGUNE, 20009 San Sebastian, Spain*

Ronald F. Ziolo − *Centro de Investigación en Química Aplicada, 25294 Saltillo, Coahuila, México*

Sergio E. Moya − *Soft Matter Nanotechnology Group, CIC biomaGUNE, 20009 San Sebastian, Spain; NanoBioMedical Centre, Adam Mickiewicz University, 61-614 Poznan, Poland;* orcid.org/0000-0002-7174-1960

Complete contact information is available at: https://pubs.acs.org/10.1021/acsnano.1c08695

Notes

The authors declare no competing financial interest.

ACKNOWLEDGMENTS

The authors acknowledge support through the ERA-NET SIINN Fatenano (PCIN-2015-116 and U.S. National Science Foundation CBET 1530790). The work was further supported by the National Science Foundation (OAC 1931587 and CMMI 1940335). We utilized the Oak Ridge Leadership

Computing Facility at the Oak Ridge National Laboratory (DE-AC05-00OR22725) and the Argonne Leadership Computing Facility (DE-AC02-06CH11357), which are supported by the Office of Science of the U.S. Department of Energy. We further acknowledge resources of the Summit supercomputer, a joint effort of the University of Colorado Boulder and Colorado State University, which is supported by the National Science Foundation (ACI 1532235 and ACI 1532236). S.E.M. also thanks the National Science Centre of Poland under the program OPUS: 2019/33/B/ST5/01495.

REFERENCES

(1) Mitchell, M. J.; Billingsley, M. M.; Haley, R. M.; Wechsler, M. E.; Peppas, N. A.; Langer, R. Engineering Precision Nanoparticles for Drug Delivery. *Nat. Rev. Drug Discovery* **2021**, *20*, 101−124.
(2) Heinz, H.; Pramanik, C.; Heinz, O.; Ding, Y.; Mishra, R. K.; Marchon, D.; Flatt, R. J.; Estrela-Lopis, I.; Llop, J.; Moya, S.; Ziolo, R. F. Nanoparticle Decoration with Surfactants: Molecular Interactions, Assembly, and Applications. *Surf. Sci. Rep.* **2017**, *72*, 1−58.
(3) Rennick, J. J.; Johnston, A. P. R.; Parton, R. G. Key Principles and Methods for Studying the Endocytosis of Biological and Nanoparticle Therapeutics. *Nat. Nanotechnol.* **2021**, *16*, 266−276.
(4) Corbo, C.; Molinaro, R.; Parodi, A.; Toledano Furman, N. E.; Salvatore, F.; Tasciotti, E. The Impact of Nanoparticle Protein Corona on Cytotoxicity, Immunotoxicity and Target Drug Delivery. *Nanomedicine (Lond)* **2016**, *11*, 81−100.
(5) Cedervall, T.; Lynch, I.; Lindman, S.; Berggard, T.; Thulin, E.; Nilsson, H.; Dawson, K. A.; Linse, S. Understanding the Nanoparticle-Protein Corona Using Methods to Quantify Exchange Rates and Affinities of Proteins for Nanoparticles. *Proc. Natl. Acad. Sci. U. S. A.* **2007**, *104*, 2050−2055.
(6) Chen, K.; Xu, Y.; Rana, S.; Miranda, O. R.; Dubin, P. L.; Rotello, V. M.; Sun, L.; Guo, X. Electrostatic Selectivity in Protein-Nanoparticle Interactions. *Biomacromolecules* **2011**, *12*, 2552−2561.
(7) Lundqvist, M.; Stigler, J.; Elia, G.; Lynch, I.; Cedervall, T.; Dawson, K. A. Nanoparticle Size and Surface Properties Determine the Protein Corona with Possible Implications for Biological Impacts. *Proc. Natl. Acad. Sci. U. S. A.* **2008**, *105*, 14265−14270.
(8) Rechendorff, K.; Hovgaard, M. B.; Foss, M.; Zhdanov, V. P.; Besenbacher, F. Enhancement of Protein Adsorption Induced by Surface Roughness. *Langmuir* **2006**, *22*, 10885−10888.
(9) Silvestri, A.; Di Silvio, D.; Llarena, I.; Murray, R. A.; Marelli, M.; Lay, L.; Polito, L.; Moya, S. E. Influence of Surface Coating on the Intracellular Behaviour of Gold Nanoparticles: A Fluorescence Correlation Spectroscopy Study. *Nanoscale* **2017**, *9*, 14730−14739.
(10) Di Silvio, D.; Silvestri, A.; Lay, L.; Polito, L.; Moya, S. E. Impact of Concanavalin A Affinity in the Intracellular Fate of Protein Corona on Glucosamine Au Nanoparticles. *Sci. Rep.* **2018**, *8*, 9046.
(11) Rabanel, J. M.; Adibnia, V.; Tehrani, S. F.; Sanche, S.; Hildgen, P.; Banquy, X.; Ramassamy, C. Nanoparticle Heterogeneity: An Emerging Structural Parameter Influencing Particle Fate in Biological Media? *Nanoscale* **2019**, *11*, 383−406.
(12) Michel, R.; Pasche, S.; Textor, M.; Castner, D. G. Influence of PEG Architecture on Protein Adsorption and Conformation. *Langmuir* **2005**, *21*, 12327−12332.
(13) Meder, F.; Daberkow, T.; Treccani, L.; Wilhelm, M.; Schowalter, M.; Rosenauer, A.; Madler, L.; Rezwan, K. Protein Adsorption on Colloidal Alumina Particles Functionalized with Amino, Carboxyl, Sulfonate and Phosphate Groups. *Acta Biomater.* **2012**, *8*, 1221−1229.
(14) Walkey, C. D.; Olsen, J. B.; Guo, H. B.; Emili, A.; Chan, W. C. W. Nanoparticle Size and Surface Chemistry Determine Serum Protein Adsorption and Macrophage Uptake. *J. Am. Chem. Soc.* **2012**, *134*, 2139−2147.
(15) Bidoggia, S.; Milocco, F.; Polizzi, S.; Canton, P.; Saccani, A.; Sanavio, B.; Krol, S.; Stellacci, F.; Pengo, P.; Pasquato, L. Fluorinated and Charged Hydrogenated Alkanethiolates Grafted on Gold: Expanding the Diversity of Mixed-Monolayer Nanoparticles for Biological Applications. *Bioconjugate Chem.* **2017**, *28*, 43−52.
(16) Gentilini, C.; Pasquato, L. Morphology of Mixed-Monolayers Protecting Metal Nanoparticles. *J. Mater. Chem.* **2010**, *20*, 1403−1412.
(17) Liu, X.; Yu, M.; Kim, H.; Mameli, M.; Stellacci, F. Determination of Monolayer-Protected Gold Nanoparticle Ligand-shell Morphology using NMR. *Nat. Commun.* **2012**, *3*, 1182.
(18) Prathima, N.; Harini, M.; Rai, N.; Chandrashekara, R. H.; Ayappa, K. G.; Sampath, S.; Biswas, S. K. Thermal Study of Accumulation of Conformational Disorders in the Self-Assembled Monolayers of C8 and C18 Alkanethiols on the Au111 Surface. *Langmuir* **2005**, *21*, 2364−2374.
(19) Tarek, M.; Tu, K.; Klein, M. L.; Tobias, D. J. Molecular Dynamics Simulations of Supported Phospholipid/Alkanethiol Bilayers on a Gold(111) Surface. *Biophys. J.* **1999**, *77*, 964−972.
(20) Vemparala, S.; Karki, B. B.; Kalia, R. K.; Nakano, A.; Vashishta, P. Large-Scale Molecular Dynamics Simulations of Alkanethiol Self-Assembled Monolayers. *J. Chem. Phys.* **2004**, *121*, 4323−4330.
(21) Fu, Y. T.; Heinz, H. Cleavage Energy of Alkylammonium-Modified Montmorillonite and Relation to Exfoliation in Nanocomposites: Influence of Cation Density, Head Group Structure, and Chain Length. *Chem. Mater.* **2010**, *22*, 1595−1605.
(22) Heinz, H.; Castelijns, H. J.; Suter, U. W. Structure and Phase Transitions of Alkyl Chains on Mica. *J. Am. Chem. Soc.* **2003**, *125*, 9500−9510.
(23) Lane, J. M. D.; Grest, G. S. Spontaneous Asymmetry of Coated Spherical Nanoparticles in Solution and at Liquid-Vapor Interfaces. *Phys. Rev. Lett.* **2010**, *104* (23), 235501.
(24) Bolintineanu, D. S.; Lane, J. M. D.; Grest, G. S. Effects of Functional Groups and Ionization on the Structure of Alkanethiol-Coated Gold Nanoparticles. *Langmuir* **2014**, *30*, 11075−11085.
(25) Lane, J. M. D.; Grest, G. S. Assembly of Responsive-Shape Coated Nanoparticles at Water Surfaces. *Nanoscale* **2014**, *6*, 5132−5137.
(26) Jimenez, A.; Sarsa, A.; Blazquez, M.; Pineda, T. A Molecular Dynamics Study of the Surfactant Surface Density of Alkanethiol Self-Assembled Monolayers on Gold Nanoparticles as a Function of the Radius. *J. Phys. Chem. C* **2010**, *114*, 21309−21314.
(27) Yan, C.; Yuan, R.; Pfalzgraff, W. C.; Nishida, J.; Wang, L.; Markland, T. E.; Fayer, M. D. Unraveling the Dynamics and Structure of Functionalized Self-Assembled Monolayers on Gold Using 2D IR Spectroscopy and MD Simulations. *Proc. Natl. Acad. Sci. U. S. A.* **2016**, *113*, 4929−4934.
(28) Mark, L. O.; Zhu, C.; Medlin, J. W.; Heinz, H. Understanding the Surface Reactivity of Ligand-Protected Metal Nanoparticles for Biomass Upgrading. *ACS Catal.* **2020**, *10*, 5462−5474.
(29) Adams, D. M.; Brus, L.; Chidsey, C. E. D.; Creager, S.; Creutz, C.; Kagan, C. R.; Kamat, P. V.; Lieberman, M.; Lindsay, S.; Marcus, R. A.; Metzger, R. M.; Michel-Beyerle, M. E.; Miller, J. R.; Newton, M. D.; Rolison, D. R.; Sankey, O.; Schanze, K. S.; Yardley, J.; Zhu, X. Y. Charge transfer on the Nanoscale: Current Status. *J. Phys. Chem. B* **2003**, *107*, 6668−6697.
(30) Love, J. C.; Estroff, L. A.; Kriebel, J. K.; Nuzzo, R. G.; Whitesides, G. M. Self-Assembled Monolayers of Thiolates on Metals As a Form of Nanotechnology. *Chem. Rev.* **2005**, *105*, 1103−1169.
(31) Zheng, J.; Li, L. Y.; Tsao, H. K.; Sheng, Y. J.; Chen, S. F.; Jiang, S. Y. Strong Repulsive Forces Between Protein and Oligo (Ethylene Glycol) Self-Assembled Monolayers: A Molecular Simulation Study. *Biophys. J.* **2005**, *89*, 158−166.
(32) Prime, K. L.; Whitesides, G. M. Adsorption of Proteins onto Surfaces Containing End-Attached Oligo(Ethylene Oxide) - a Model System Using Self-Assembled Monolayers. *J. Am. Chem. Soc.* **1993**, *115*, 10714−10721.
(33) Mrksich, M.; Whitesides, G. M. Using Self-Assembled Monolayers that Present Oligo(ethylene glycol) Groups to Control the Interactions of Proteins with Surfaces. *ACS Symposium Series Poly(Ethylene Glycol)* **1997**, *680*, 361−373.

https://doi.org/10.1021/acsnano.1c08695
ACS Nano 2022, 16, 8766−8783

(34) Frederix, F.; Bonroy, K.; Laureyn, W.; Reekmans, G.; Campitelli, A.; Dehaen, W.; Maes, G. Enhanced Performance of an Affinity Biosensor Interface Based on Mixed Self-Assembled Monolayers of Thiols on Gold. *Langmuir* **2003**, *19*, 4351−4357.
(35) Stranick, S. J.; Parikh, A. N.; Tao, Y. T.; Allara, D. L.; Weiss, P. S. Phase-Separation of Mixed-Composition Self-Assembled Monolayers into Nanometer-Scale Molecular Domains. *J. Phys. Chem.* **1994**, *98*, 7636−7646.
(36) Singh, C.; Ghorai, P. K.; Horsch, M. A.; Jackson, A. M.; Larson, R. G.; Stellacci, F.; Glotzer, S. C. Entropy-Mediated Patterning of Surfactant-Coated Nanoparticles and Surfaces. *Phys. Rev. Lett.* **2007**, *99*, 226106.
(37) Velachi, V.; Bhandary, D.; Singh, J. K.; Cordeiro, M. N. D. S. Structure of Mixed Self-Assembled Monolayers on Gold Nanoparticles at Three Different Arrangements. *J. Phys. Chem. C* **2015**, *119*, 3199−3209.
(38) Van Lehn, R. C.; Alexander-Katz, A. Structure of Mixed-Monolayer-Protected Nanoparticles in Aqueous Salt Solution from Atomistic Molecular Dynamics Simulations. *J. Phys. Chem. C* **2013**, *117*, 20104−20115.
(39) Huang, R. X.; Carney, R. R.; Ikuma, K.; Stellacci, F.; Lau, B. L. T. Effects of Surface Compositional and Structural Heterogeneity on Nanoparticle-Protein Interactions: Different Protein Configurations. *ACS Nano* **2014**, *8*, 5402−5412.
(40) Huang, R. X.; Carney, R. P.; Stellacci, F.; Lau, B. L. T. Protein-Nanoparticle Interactions: The Effects of Surface Compositional and Structural Heterogeneity are Scale Dependent. *Nanoscale* **2013**, *5*, 6928−6935.
(41) Van Lehn, R. C.; Alexander-Katz, A. Pathway for Insertion of Amphiphilic Nanoparticles into Defect-Free Lipid Bilayers from Atomistic Molecular Dynamics Simulations. *Soft Matter* **2015**, *11*, 3165−3175.
(42) Van Lehn, R. C.; Atukorale, P. U.; Carney, R. P.; Yang, Y. S.; Stellacci, F.; Irvine, D. J.; Alexander-Katz, A. Effect of Particle Diameter and Surface Composition on the Spontaneous Fusion of Monolayer-Protected Gold Nanoparticles with Lipid Bilayers. *Nano Lett.* **2013**, *13*, 4060−4067.
(43) Centrone, A.; Penzo, E.; Sharma, M.; Myerson, J. W.; Jackson, A. M.; Marzari, N.; Stellacci, F. The Role of Nanostructure in the Wetting Behavior of Mixed-Monolayer-Protected Metal Nanoparticles. *Proc. Natl. Acad. Sci. U.S.A.* **2008**, *105*, 9886−9891.
(44) Beddoes, C. M.; Case, C. P.; Briscoe, W. H. Understanding Nanoparticle Cellular Entry: A Physicochemical Perspective. *Adv. Colloid Interface Sci.* **2015**, *218*, 48−68.
(45) Stirling, J.; Lekkas, I.; Sweetman, A.; Djuranovic, P.; Guo, Q.; Pauw, B.; Granwehr, J.; Levy, R.; Moriarty, P. Critical Assessment of the Evidence for Striped Nanoparticles. *PloS one* **2014**, *9*, e108482.
(46) Cesbron, Y.; Shaw, C. P.; Birchall, J. P.; Free, P.; Levy, R. Stripy Nanoparticles Revisited. *Small* **2012**, *8*, 3714−3719.
(47) Yu, M.; Stellacci, F. Response to ″Stripy Nanoparticles Revisited. *Small* **2012**, *8*, 3720−3726.
(48) Fetisov, E. O.; Siepmann, J. I. Structure and Phase Behavior of Mixed Self-Assembled Alkanethiolate Monolayers on Gold Nanoparticles: A Monte Carlo Study. *J. Phys. Chem. B* **2016**, *120*, 1972−1978.
(49) Gkeka, P.; Sarkisov, L.; Angelikopoulos, P. Homogeneous Hydrophobic-Hydrophilic Surface Patterns Enhance Permeation of Nanoparticles through Lipid Membranes. *J. Phys. Chem. Lett.* **2013**, *4*, 1907−1912.
(50) Heinz, H.; Lin, T.-J.; Kishore Mishra, R.; Emami, F. S. Thermodynamically Consistent Force Fields for the Assembly of Inorganic, Organic, and Biological Nanostructures: The INTERFACE Force Field. *Langmuir* **2013**, *29*, 1754−1765.
(51) Liu, J.; Zeng, J.; Zhu, C.; Miao, J.; Huang, Y.; Heinz, H. Interpretable Molecular Models for Molybdenum Disulfide and Insight into Selective Peptide Recognition. *Chem. Sci.* **2020**, *11*, 8708−8722.
(52) Kanhaiya, K.; Kim, S.; Im, W.; Heinz, H. Accurate Simulation of Surfaces and Interfaces of Ten FCC Metals and Steel Using Lennard−Jones Potentials. *NPJ. Comput. Mater.* **2021**, *7*, 17.
(53) Mark, L. O.; Zhu, C.; Medlin, J. W.; Heinz, H. Understanding the Surface Reactivity of Ligand-Protected Metal Nanoparticles for Biomass Upgrading. *ACS Catal.* **2020**, *10*, 5462−5474.
(54) Nathanson, M.; Kanhaiya, K.; Pryor, A.; Miao, J.; Heinz, H. Atomic-Scale Structure and Stress Release Mechanism in Core−Shell Nanoparticles. *ACS Nano* **2018**, *12*, 12296−12304.
(55) Pramanik, C.; Jamil, T.; Gissinger, J. R.; Guittet, D.; Arias-Monje, P. J.; Kumar, S.; Heinz, H. Polyacrylonitrile Interactions with Carbon Nanotubes in Solution: Conformations and Binding As a Function of Solvent, Temperature, and Concentration. *Adv. Funct. Mater.* **2019**, *29*, 1905247.
(56) Retout, M.; Brunetti, E.; Valkenier, H.; Bruylants, G. Limits of Thiol Chemistry Revealed by Quantitative Analysis of Mixed Layers of Thiolated-PEG Ligands Grafted onto Gold Nanoparticles. *J. Colloid Interface Sci.* **2019**, *557*, 807−815.
(57) Hinterwirth, H.; Kappel, S.; Waitz, T.; Prohaska, T.; Lindner, W.; Lämmerhofer, M. Quantifying Thiol Ligand Density of Self-Assembled Monolayers on Gold Nanoparticles by Inductively Coupled Plasma−Mass Spectrometry. *ACS Nano* **2013**, *7*, 1129−1136.
(58) Lu, J.; Xue, Y.; Shi, R.; Kang, J.; Zhao, C.-Y.; Zhang, N.-N.; Wang, C.-Y.; Lu, Z.-Y.; Liu, K. A Non-Sacrificial Method for the Quantification of Poly(ethylene glycol) Grafting Density on Gold Nanoparticles for Applications in Nanomedicine. *Chem. Sci.* **2019**, *10*, 2067−2074.
(59) Tong, L.; Lu, E.; Pichaandi, J.; Cao, P. P.; Nitz, M.; Winnik, M. A. Quantification of Surface Ligands on NaYF4 Nanoparticles by Three Independent Analytical Techniques. *Chem. Mater.* **2015**, *27*, 4899−4910.
(60) Torelli, M. D.; Putans, R. A.; Tan, Y.; Lohse, S. E.; Murphy, C. J.; Hamers, R. J. Quantitative Determination of Ligand Densities on Nanomaterials by X-ray Photoelectron Spectroscopy. *ACS Appl. Mater. Interfaces* **2015**, *7*, 1720−1725.
(61) Lin, J. Q.; Zhang, H.; Morovati, V.; Dargazany, R. PEGylation on Mixed Monolayer Gold Nanoparticles: Effect of Grafting Density, Chain Length, and Surface Curvature. *J. Colloid Interface Sci.* **2017**, *504*, 325−333.
(62) Takahashi, Y.; Tadokoro, H. Structural Studies of Polyethers, (-(CH2)m-O-)n. X. Crystal Structure of Poly(ethylene oxide). *Macromolecules* **1973**, *6*, 672−675.
(63) Heinz, H.; Vaia, R. A.; Farmer, B. L. Relation Between Packing Density and Thermal Transitions of Alkyl Chains on Layered Silicate and Metal Surfaces. *Langmuir* **2008**, *24*, 3727−3733.
(64) Ghorai, P. K.; Glotzer, S. C. Molecular Dynamics Simulation Study of Self-Assembled Monolayers of Alkanethiol Surfactants on Spherical Gold Nanoparticles. *J. Phys. Chem. C* **2007**, *111*, 15857−15862.
(65) Degennes, P. G. Polymers at an Interface - a Simplified View. *Adv. Colloid Interface Sci.* **1987**, *27*, 189−209.
(66) Vericat, C.; Vela, M. E.; Benitez, G.; Carro, P.; Salvarezza, R. C. Self-Assembled Monolayers of Thiols and Dithiols on Gold: New Challenges for a Well-Known System. *Chem. Soc. Rev.* **2010**, *39*, 1805−1834.
(67) Vericat, C.; Vela, M. E.; Benitez, G. A.; Gago, J. A. M.; Torrelles, X.; Salvarezza, R. C. Surface Characterization of Sulfur and Alkanethiol Self-Assembled Monolayers on Au(111). *J. Phys.: Condens. Matter* **2006**, *18*, R867−R900.
(68) Guerrini, L.; Alvarez-Puebla, R. A.; Pazos-Perez, N. Surface Modifications of Nanoparticles for Stability in Biological Fluids. *Materials* **2018**, *11*, 1154.
(69) Heinz, H.; Suter, U. W. Surface Structure of Organoclays. *Angew. Chem.-Int. Ed.* **2004**, *43*, 2239−2243.
(70) Boese, R.; Weiss, H. C.; Blaser, D. The Melting Point Alternation in the Short-Chain n-Alkanes: Single-Crystal X-ray Analyses of Propane at 30 K and of n-Butane to n-Nonane at 90 K. *Angew. Chem.-Int. Ed.* **1999**, *38*, 988−992.

https://doi.org/10.1021/acsnano.1c08695
ACS Nano 2022, 16, 8766−8783

(71) Chen, J.; Zhu, E.; Liu, J.; Zhang, S.; Lin, Z.; Duan, X.; Heinz, H.; Huang, Y.; De Yoreo, J. J. Building Two-Dimensional Materials One Row at a Time: Avoiding the Nucleation Barrier. *Science* **2018**, *362*, 1135−1139.
(72) Stefanakis, D.; Harmandaris, V.; Kopidakis, G.; Remediakis, I. From Order to Disorder of Alkanethiol Self-Assembled Monolayers on Complex Au (211), (221), and (311) Surfaces: Impact of the Substrate. *J. Phys. Chem. C* **2021**, *125*, 3495−3508.
(73) Rahme, K.; Chen, L.; Hobbs, R. G.; Morris, M. A.; O'Driscoll, C.; Holmes, J. D. PEGylated Gold Nanoparticles: Polymer Quantification as a Function of PEG Lengths and Nanoparticle Dimensions. *RSC Adv.* **2013**, *3*, 6085−6094.
(74) Garley, A.; Arias-Monje, P. J.; Hoff, S. E.; Sharp, M.; Kumar, S.; Heinz, H. Interaction of Poly(methyl acrylate) with Carbon Nanotubes as a Function of CNT Diameter, Chirality, and Temperature. *J. Phys. Chem. C* **2020**, *124*, 25632−25644.
(75) Ghorai, P. K.; Glotzer, S. C. Atomistic Simulation Study of Striped Phase Separation in Mixed-Ligand Self-Assembled Monolayer Coated Nanoparticles. *J. Phys. Chem. C* **2010**, *114*, 19182−19187.
(76) Sekiguchi, S.; Niikura, K.; Matsuo, Y.; Ijiro, K. Hydrophilic Gold Nanoparticles Adaptable for Hydrophobic Solvents. *Langmuir* **2012**, *28*, 5503−5507.
(77) Penna, M.; Ley, K.; Maclaughlin, S.; Yarovsky, I. Surface Heterogeneity: A Friend or Foe of Protein Adsorption - Insights from Theoretical Simulations. *Farad. Disc.* **2016**, *191*, 435−464.
(78) Penna, M.; Ley, K. J.; Belessiotis-Richards, A.; MacLaughlin, S.; Winkler, D. A.; Yarovsky, I. Hydration and Dynamics of Ligands Determine the Antifouling Capacity of Functionalized Surfaces. *J. Phys. Chem. C* **2019**, *123*, 30360−30372.
(79) Van Lehn, R. C.; Alexander-Katz, A. Penetration of Lipid Bilayers by Nanoparticles with Environmentally-Responsive Surfaces: Simulations and Theory. *Soft Matter* **2011**, *7*, 11392−11404.
(80) Verma, A.; Uzun, O.; Hu, Y. H.; Hu, Y.; Han, H. S.; Watson, N.; Chen, S. L.; Irvine, D. J.; Stellacci, F. Surface-Structure-Regulated Cell-Membrane Penetration by Monolayer-Protected Nanoparticles. *Nat. Mater.* **2008**, *7*, 588−595.
(81) Rabbani, G.; Ahn, S. N. Structure, Enzymatic Activities, Glycation and Therapeutic Potential of Human Serum Albumin: A Natural Cargo. *Int. J. Biol. Macromol.* **2019**, *123*, 979−990.
(82) Liu, Z. B.; Chen, X. Y. Simple Bioconjugate Chemistry Serves Great Clinical Advances: Albumin as a Versatile Platform for Diagnosis and Precision Therapy. *Chem. Soc. Rev.* **2016**, *45*, 1432−1456.
(83) Dallin, B. C.; Van Lehn, R. C. Spatially Heterogeneous Water Properties at Disordered Surfaces Decrease the Hydrophobicity of Nonpolar Self-Assembled Monolayers. *J. Phys. Chem. Lett.* **2019**, *10*, 3991−3997.
(84) Prime, K. L.; Whitesides, G. M. Self-Assembled Organic Monolayers - Model Systems for Studying Adsorption of Proteins at Surfaces. *Science* **1991**, *252*, 1164−1167.
(85) Krishna, A. D. S.; Mandraju, R. K.; Kishore, G.; Kondapi, A. K. An Efficient Targeted Drug Delivery through Apotransferrin Loaded Nanoparticles. *PloS one* **2009**, *4*, e7240.
(86) Piraux, H.; Hai, J.; Verbeke, P.; Serradji, N.; Ammar, S.; Losno, R.; Ha-Duong, N.-T.; Hemadi, M.; El Hage Chahine, J.-M. Transferrin Receptor-1 Iron-Acquisition Pathway - Synthesis, Kinetics, Thermodynamics and Rapid Cellular Internalization of a Holotransferrin-Maghemite Nanoparticle Construct. *Biochim. Biophys. Acta* **2013**, *1830*, 4254−4264.
(87) *Materials Studio 2019 Program Suite and User Guide*; Biovia/Dassault Systemes: Cambridge, UK, 2019.
(88) Coppage, R.; Slocik, J. M.; Ramezani-Dakhel, H.; Bedford, N. M.; Heinz, H.; Naik, R. R.; Knecht, M. R. Exploiting Localized Surface Binding Effects to Enhance the Catalytic Reactivity of Peptide-Capped Nanoparticles. *J. Am. Chem. Soc.* **2013**, *135*, 11048−11054.
(89) Majorek, K. A.; Porebski, P. J.; Dayal, A.; Zimmerman, M. D.; Jablonska, K.; Stewart, A. J.; Chruszcz, M.; Minor, W. Structural and Immunologic Characterization of Bovine, Horse, and Rabbit Serum Albumins. *Mol. Immunol.* **2012**, *52*, 174−182.
(90) Geada, I. L.; Ramezani-Dakhel, H.; Jamil, T.; Sulpizi, M.; Heinz, H. Insight into Induced Charges at Metal Surfaces and Biointerfaces Using a Polarizable Lennard-Jones Potential. *Nat. Commun.* **2018**, *9*, 716.
(91) Lin, T. J.; Heinz, H. Accurate Force Field Parameters and pH Resolved Surface Models for Hydroxyapatite to Understand Structure, Mechanics, Hydration, and Biological Interfaces. *J. Phys. Chem. C* **2016**, *120*, 4975−4992.
(92) Phillips, J. C.; Braun, R.; Wang, W.; Gumbart, J.; Tajkhorshid, E.; Villa, E.; Chipot, C.; Skeel, R. D.; Kale, L.; Schulten, K. Scalable Molecular Dynamics with NAMD. *J. Comput. Chem.* **2005**, *26*, 1781−1802.
(93) Huang, J.; MacKerell, A. D. CHARMM36 All-Atom Additive Protein Force Field: Validation Based on Comparison to NMR Data. *J. Comput. Chem.* **2013**, *34*, 2135−2145.
(94) Heinz, H.; Vaia, R. A.; Farmer, B. L.; Naik, R. R. Accurate Simulation of Surfaces and Interfaces of Face-Centered Cubic Metals Using 12−6 and 9−6 Lennard-Jones Potentials. *J. Phys. Chem. C* **2008**, *112*, 17281−17290.
(95) Fu, Y. T.; Zartman, G. D.; Yoonessi, M.; Drummy, L. F.; Heinz, H. Bending of Layered Silicates on the Nanometer Scale: Mechanism, Stored Energy, and Curvature Limits. *J. Phys. Chem. C* **2011**, *115*, 22292−22300.
(96) Briggs, B.; Bedford, N. M.; Seifert, S.; Koerner, H.; Ramezani-Dakhel, H.; Heinz, H.; Naik, R. R.; Frenkel, A.; Knecht, M. R. Atomic-Scale Identification of Pd Leaching in Nanoparticle Catalyzed CC Coupling: Effects of Particle Surface Disorder. *Chem. Sci.* **2015**, *6*, 6413−6419.
(97) Ruan, L. Y.; Ramezani-Dakhel, H.; Lee, C.; Li, Y. J.; Duan, X. F.; Heinz, H.; Huang, Y. A Rational Biomimetic Approach to Structure Defect Generation in Colloidal Nanocrystals. *ACS Nano* **2014**, *8*, 6934−6944.
(98) Vanommeslaeghe, K.; Hatcher, E.; Acharya, C.; Kundu, S.; Zhong, S.; Shim, J.; Darian, E.; Guvench, O.; Lopes, P.; Vorobyov, I.; MacKerell, A. D. CHARMM General Force Field: A Force Field for Drug-Like Molecules Compatible with the CHARMM All-Atom Additive Biological Force Fields. *J. Comput. Chem.* **2010**, *31*, 671−690.
(99) *CRC Handbook of Chemistry and Physics*, 101st ed.; Rumble, J. R., Ed.; CRC Press: Boca Raton, FL, 2020.
(100) Wang, S.; Hou, K.; Heinz, H. Accurate Compatible Force Fields for Molecular Oxygen, Nitrogen and Hydrogen to Simulate Heterogeneous Electrolytes and Interfaces. *J. Chem. Theory Comput.h* **2021**, *17*, 5198−5213.
(101) Humphrey, W.; Dalke, A.; Schulten, K. VMD: Visual Molecular Dynamics. *J. Mol. Graph. Model* **1996**, *14*, 33−38.

https://doi.org/10.1021/acsnano.1c08695
ACS Nano 2022, 16, 8766−8783